

Spectral Data Analysis of X-Ray Binary: 4U 1543-47

An internship report submitted
in partial fulfillment for the award of the degree of

Bachelor of Technology

in

Engineering Physics

by

Kanishka Arora



**Department of Physics Department
Indian Institute of Space Science and Technology
Thiruvananthapuram, India**

Month Year

Certificate

This is to confirm that the internship report titled Internship Report on Spectral Data Analysis of X-Ray Binaries using xspec software submitted by **Kanishka Arora** to the **Indian Institute of Space Science and Technology**, Thiruvananthapuram, as part of the requirements for the degree of Bachelor of Technology in Engineering Physics, represents an authentic account of the original work conducted by the student under my supervision. The entirety or portions of this internship report have not been presented to any other institute or university for the purpose of obtaining any degree or diploma.

Dr.Samir Mandal,
Professor

Dr. Rama Rao Nidamanuri
Professor Head of Department
Department of Earth and Space Sciences

Place: Thiruvananthapuram
Date: November 2022

Declaration

I declare that this internship report titled ***Spectral Data Analysis of X-Ray Binary: 4U 1543-47*** submitted in partial fulfillment for the award of the degree of **Bachelor of Technology in Engineering Physics** is a record of the original work carried out by me under the supervision of **Samir Mandal**, and has not formed the basis for the award of any degree, diploma, associateship, fellowship, or other titles in this or any other Institution or University of higher learning. In keeping with the ethical practice in reporting scientific information, due acknowledgments have been made wherever the findings of others have been cited.

Place: Thiruvananthapuram

Kanishka Arora

5mm

Date: November 2023

This internship report is dedicated to my parents who have always supported me throughout my journey. I would also like to appreciate the effort put in by the professors at IIEST who are very keen on helping the growth of students. Special thanks to Dr.Samir Mandal who was the guide of my internship project.

Acknowledgements

First and foremost, I would like to acknowledge the excellent guidance from Dr.Samir Mandal, a Distinguished Professor, the Indian Institute of Space Science and Technology. I would like to thank him for giving me the opportunity to offer me an internship project this summer which gave me a broad idea about the field of Astronomy and Astrophysics.

I would also like to thank Dr.Geethu Prabhakar, who recently got her P.H.D diploma this year from IIST under Dr.Samir Mandal. She helped on the basic foundations involved for the project and gave me material to go through as well. Her knowledge on the usage of the xspec software was very helpful to me during my internship.

Kanishka Arora

Abstract

Well, we all know what **Black-Holes** are all about. Since our younger classes, we have been hearing about Black-Holes and the matter-sucking objects they are in space. It was a very hot topic(still is) that intrigued us all, because how can such objects even exist in space? Well, this is one reason why I pursued my summer internship in this area. And partly also because I am inclined towards the domain of **High Energy Astrophysics**.

In this internship report, you will further read that I have used the **xspec** software which is included while installing **HEASOFT** to model the spectral data from the **NuSTAR** instruments A and B. The source here is an X-ray binary going by the name of 4U 1543-47. At the time of analysis, there were 10 public **NuSTAR** observations of which were all taken in the 2021 outburst, with the source flux decreasing in each new observation.

I have used models such as **tbabs**, **diskbb**, **zxipcf**, and **relxill**. All these models are available in **xspec** except for the last one which has to be separately installed through the **relxill** website. Using a combination of these models, I have tried to get the best possible fit for the observed spectral data and obtain the best-fit parameters. After getting the best possible fit I run MCMC(Markov Chain Monte Carlo) chains for each observation to calculate the error range for all the parameters involved.

Contents

1	Introduction	1
1.1	Black Holes	1
1.2	X-Ray Binaries:	3
2	Physics involved in Binary Systems	7
2.1	Different components of the X-Ray spectrum	7
2.2	Physical processes which are occurring in the accretion disk/corona system	10
2.3	States of the Source	13
3	X-Ray Astronomy	16
3.1	Missions based on X-Ray Astronomy	16
3.2	NuSTAR Mission	19
4	Data Analysis	22
4.1	A little background on XSPEC	22
4.2	Basics of Spectral fitting	23
4.3	Implementation	26
4.4	Some Basic Commands	27
5	Studying 4U 1543-47 outbursts	30
5.1	Introduction	30
5.2	Relxill Component	31
5.3	Markov Chain Monte Carlo (MCMC)	33
5.4	Models and Parameters used for this source	34
5.5	Observations	37
6	Bibliography and References	65

Chapter 1

Introduction

1.1 Black Holes

Black Holes were almost discovered around 132 years ago, in 1915, when Karl Schwarzschild found a solution in general relativity. They are mysterious yet, from a physics perspective, can be considered simple.

A black hole is characterized mainly by two parameters: mass (M) and angular momentum (J). The electric charge (Q) is often considered null, as any net charge attracts opposite charges.

Born from a star's nuclear fuel depletion, a black hole forms through gravitational collapse, compressing matter into a singularity. The structure details are calculated from Einstein's general relativity, with credit to Karl Schwarzschild. His solution introduced the Schwarzschild radius.

A black hole is fully characterized by mass (M) and specific angular momentum (J or spin a). The spin parameter (a_*) ranges from 0 for a Schwarzschild hole to 1 for a maximally rotating Kerr hole.

Schwarzschild black holes

A non-rotating, uncharged black hole (with $J = Q = 0$) is termed a Schwarzschild black hole. Formed from the gravitational collapse of mass (M) within a sphere with a radius R_{Sch} , a Schwarzschild black hole has an event horizon (R_H) equal to its Schwarzschild radius (R_{Sch}).

In the context of Active Galactic Nuclei (AGN), a black hole with a mass of $M = 10^8$ solar masses has $R_{\text{Sch}} = 3 \times 10^8$ km, while a stellar-mass black hole with $M = 3$ solar masses has $R_{\text{Sch}} = 9$ km. The material being accreted orbits the black hole before

crossing the Schwarzschild radius. In general relativity, the innermost stable circular orbit (R_{ISCO}) for Schwarzschild black holes is three times the distance from the event horizon, i.e., $R_{\text{ISCO}} = 3R_{\text{Sch}}$.

Kerr black holes

Stars, while rotating with a considerable amount of angular momentum, retain this rotational energy in their remnants after their demise, unless there is an effective mechanism slowing them down. Einstein's field equations offer the Schwarzschild solution for non-rotating black holes, and this solution can be extended to describe rotating black holes known as Kerr black holes. The Kerr metric, which characterizes these black holes, depends on both the mass and angular momentum.

The singularity discussed earlier is situated at the center of the black hole, hidden behind the event horizon. Upon entering the black hole, it becomes evident that the escape velocity in this region surpasses the speed of light, preventing even rays of light from escaping.

Now we'll talk about the classification based on mass.

1.1.1 Supermassive Black Holes:

Supermassive black holes, denoted by a mass (M) greater than 10 times that of the Sun, typically reside at the center of most galaxies in our universe. The term "supermassive" distinguishes them from smaller stellar-mass black holes, which form as a result of massive star collapses. The origin of supermassive black holes remains unclear, and scientists employ simulations to gain insights into their formation and their role within galaxies.

As matter falls into these black holes, it forms a hot and dense accretion disk, releasing an immense amount of energy in the form of X-rays and other types of radiation. Investigating these phenomena through simulations and observations contributes to our understanding of the behavior and impact of supermassive black holes within the vast cosmic structures that surround us.

1.1.2 Stellar-Mass Black holes:

Stellar-mass black holes emerge at the conclusion of a massive star's life. As noted in the preceding paragraph, they differ from supermassive black holes, which are considerably more massive.

These black holes are formed through gravitational collapse when a star lacks sufficient nuclear fuel to counterbalance gravitational forces. Stellar-mass black holes typically possess masses ranging from a few to several times that of our Sun.

1.1.3 Intermediate-Mass Black Holes:

These type of black holes have their mass ranging greater than that of stellar mass black holes and smaller than that of Supermassive Black Holes($M = 12$ to 14 SOLAR MASSES). There is active research and investigation in this area of black holes primarily because of the fact that they are harder to detect. This is due to the reason that they are expected to be less luminous compared to other sources.

There have been some astronomical objects that researchers have studied that can identify as candidates, like certain ULXs (Ultraluminous X-rays) and beamed emission from certain accreting black holes.

1.2 X-Ray Binaries:

The existence of Black-Holes comes through the study of AGN(Active Galactic Nuclei), X-ray binaries, or pulsars. which are among the brightest X-ray sources in the observable sky.

Binary systems are prevalent due to the star formation process, leading to the close proximity of proto-stars. In these systems, a compact object (e.g., a black hole, neutron star) accretes matter from its normal star companion, forming an accretion disk. High-energy processes around the compact object release gravitational potential energy, predominantly in the X-ray region.

X-rays result from particles near the compact object in the accretion disk moving at relativistic speeds, close to the speed of light. As these particles accrete into the compact

object, collisions with other particles lead to high-energy interactions. The friction and heating between particles at these high temperatures in the accretion disk cause the emission of X-rays. Now we'll talk about the kinds of X-ray Binaries.

1.2.1 Low Mass X-Ray Binaries

In LMXBs, material is pulled onto the compact object through Roche lobe overflow using an accretion disk. The formation of Low Mass X-ray Binaries (LMXBs) can occur through two distinct processes:

1.2.1.1 Two stars may be gravitationally bound by birth

In this scenario, the larger star rapidly evolves into the giant phase, leading to the transfer or expulsion of a significant part of its outer layer as the companion moves inward. Subsequently, the larger star undergoes a supernova explosion. If less than half of the binary mass is lost during this event, the binary system survives. Conversely, losing more than half of the binary mass allows survival only if a kick velocity from the explosion occurs in the correct direction.

1.2.1.2 The system may be formed by the capture of a second star

In this scenario, a solitary massive star independently evolves into a compact object, and the presence of a nearby star can lead to capture, especially in environments with high star density. Below we'll talk about the Roche lobe phenomenon more.

The Roche lobe, a teardrop-shaped region, represents the gravitational influence around each star in a binary system. This area is defined by the combined gravitational potentials of both stars and their separation distance. When a star expands beyond its Roche lobe, either through stellar evolution or other influences, outer material from the star can stream through the inner Lagrange point (the point where the gravitational forces in the system balance to zero). Since this material is no longer gravitationally bound to the star, it is transferred to the other companion star.

In a reference frame rotating with the binary system, a test mass m in the system is subjected to a force $F = -m\nabla\Phi_R$, expressed in terms of the Roche potential Φ_R :

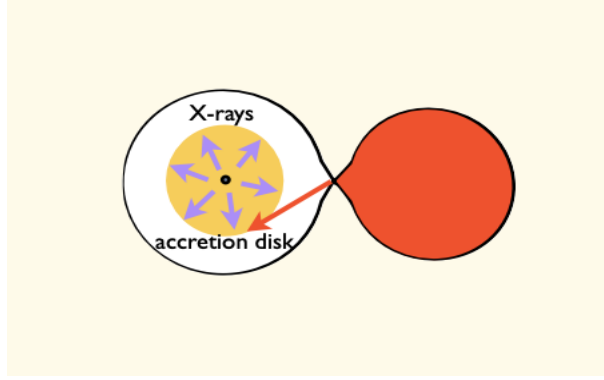


Figure 1.1: Roche Lobe Phenomenon

$$\Phi_R(r) = -\frac{GM_1}{|r - r_1|} - \frac{GM_2}{|r - r_2|} - \frac{1}{2}(w \times (r - r_c))^2,$$

r_1 = distance from center of mass M1

r_2 = distance from center of mass M2

w = angular velocity of the binary system with respect to an initial frame

$$w = \left(\frac{G(M_1+M_2)}{a^3} \right)^{1/2}$$

a = binary star separation

The transferred matter, carrying a significant amount of angular momentum, forms an accretion disk around the compact object rather than being accreted radially. Typically, the donor star in these systems is a less massive star, such as a main-sequence star or a subgiant.

1.2.2 High Mass X-Ray Binaries

HMXBs, initially observed by the UHURU mission in the 1970s, primarily accrete matter through stellar winds—fast streams of particles ejected from a star. While Roche lobe overflow contributes to accretion, it becomes unstable after 105 years if the ratio between the mass of the compact object and the mass of the companion star exceeds unity. The donor star in these systems is typically an O or B-type giant, and these binaries are commonly located in regions of active star formation. They consist of two stars that are in orbit around a common center of mass. The more massive one evolves faster and reaches the end of its

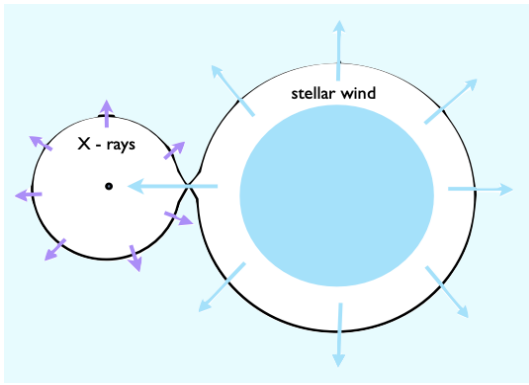


Figure 1.2: Stellar wind

life first, after a few million years or so. It becomes a giant and the outer layers are lost to its companion.

Chapter 2

Physics involved in Binary Systems

In this section, we will discuss the physics of the Binary Systems.

2.1 Different components of the X-Ray spectrum

X-ray spectra from accreting binary systems usually show a soft-thermal component, resembling a blackbody, linked to the accretion disk. Additionally, there is a hard X-ray component that tends to dominate the spectrum. This hard component is believed to arise from soft photons emitted by the disk, undergoing Compton upscattering by high-energy electrons, forming a structure known as a corona.

This component can be modeled using either a power law with a high-energy cutoff, particularly when the source is in the hard state, or a blackbody when the source is in the soft state. In the spectra of these sources, a reflection component is frequently observed, believed to result from the interaction between the Comptonized photons and the cold matter present in the accretion disk.

2.1.1 Accretion

The accretion disk is mainly composed of stellar plasma derived from the companion star, which is an ionized gas characterized by its ions and molecules.

The properties of the ions depend on the temperature of the region; the ion can be fully ionized at higher temperatures or recombine to form neutral atoms at lower temperatures. According to our theories, the structure and geometry of the accretion disk are significantly influenced by the mass accretion rate and viscosity.

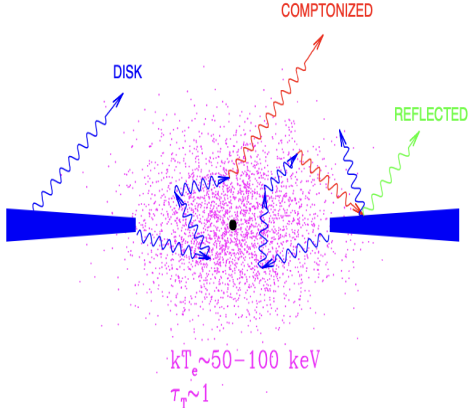


Figure 2.1: Different components of X-Ray spectrum

Various solutions to the equations of accretion flow derived from our simulations exist around the compact object, resulting in multiple models to interpret the same. Different classes of models can be distinguished, including accretion flows that are radiatively efficient and radiatively inefficient. This classification is primarily based on the following three criteria -

- The ratio between the rate of heating and the rate of cooling
- The Opacity of Gas
- The predominant pressure (gas or radiation)

Whatever the configuration, they all involve an optically thick geometrically thin accretion disk.

2.1.2 The Corona

The corona, with its high-temperature electrons exceeding 10^9 K contrasts sharply with the colder accretion disk. This temperature disparity is crucial for the corona's role in generating a high-energy spectrum through Comptonization. Energetic electrons in the corona concentrate at key regions atop and beneath the accretion disk, deviating from models like ADAFs. ADAFs propose that the inner part of the accretion disk becomes optically thin and is replaced by a hot flow.

Various theoretical models explain the existence of the corona. One suggests it forms

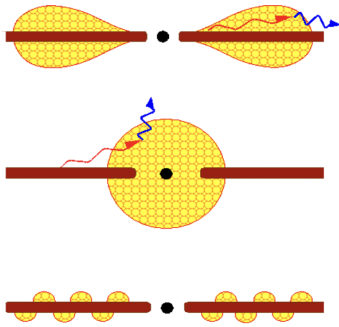


Figure 2.2: Coronal Geometries

through the evaporation of hot material from the accretion disk's surface, while another proposes energy injection from the accretion disk into an outer, less dense layer to create a hot corona. Magnetic reconnections in this process may yield a highly heated, magnetically-confined structured corona, resembling the solar corona.

Moreover, the geometry of the corona is still pretty uncertain. There are three main possible configurations-

- A "**slab**" or "sandwich" geometry, positioned above and below the accretion disk in the plane-parallel configuration.
- A "**sphere**" geometry surrounding the compact object (ADAF-like).
- A "**patchy**" or "pillbox" corona

The below figure will explain the same following.

2.1.2.1 Accretion disk corona (ADC)

In this model, there is a standard accretion disk, a structure where material spirals inward toward a compact object. This accretion disk is characterized as optically thick (meaning it doesn't allow much light to pass through) and geometrically thin (having a small vertical extent). Importantly, this accretion disk extends close to the compact object, such as a black hole or neutron star.

The unique aspect of the ADC model involves the presence of a corona. This corona is

not part of the accretion disk but is situated above and below it. The corona consists of two plane-parallel layers of hot plasma. The interaction between the accretion disk and the corona in the ADC model is proposed to be responsible for producing the observed spectral features in AGNs and X-ray binaries.

Overall, the ADC model offers a simplified yet effective framework for explaining the complex phenomena observed in these astrophysical systems.

2.1.2.2 Truncated Disk Model

In this model, the traditional thin accretion disk is truncated near the central compact object, and replaced by an inner Advection-Dominated Accretion Flow (ADAF). ADAFs prioritize heat advection, with a significant portion of generated energy carried inward rather than radiated away, resulting in low-density and high-temperature conditions.

At low accretion rates, a radiatively inefficient ADAF coexists with an outer thin accretion disk. Higher accretion rates trigger a transition in the ADAF to a more luminous, radiatively efficient state, contracting in size. The thin accretion disk moves closer to the central object, explaining spectral changes with varying mass accretion rates. This paragraph introduces the truncated disk model, emphasizing its explanatory power for system spectral changes.

2.2 Physical processes which are occurring in the accretion disk/corona system

We have discussed that the accretion disk and the corona form a complex system. These regions, where the hot corona and the cold matter disk are in close proximity, experience important interactions. The focus is on high-energy photons interacting with various particles, including atoms, nuclei, and electrons. Three primary processes are identified:

- **Photoelectric absorption**, where photons are absorbed by matter
- **Compton scattering**, where photons transfer some of their energy to electrons
- **Electron-positron pair production**, where high-energy photons can create particle-antiparticle pairs.

These processes compete with each other in terms of their efficiency in cooling the medium at specific energy levels. The efficiency of cooling is closely linked to the likelihood of these interactions, and this connection is directly related to the cross-sections of interaction. Cross-sections represent the probability of interaction occurring between particles.

2.2.1 Compton scattering - Comptonization

Inverse Compton scattering, essential in shaping the high-energy spectrum of compact objects, raises the question of how a thermal distribution of electrons leads to a power-law spectrum. The explanation involves considering multiple orders of Compton scattering, where each order corresponds to a single process. When these orders are not widely separated in energy, their contributions superimpose, resulting in a smooth power-law spectrum. This interaction of high-energy photons with a thermal electron distribution creates a power-law shape, categorized into different regimes discussed below.

2.2.1.1 Compton Scattering

Compton scattering, a quantum phenomenon, occurs when photons interact with electrons at comparable or higher energy levels, exhibiting non-classical effects. Quantum modifications in the collision's kinematics introduce angle dependence within the Klein-Nishina regime, described by the Klein–Nishina formula for scattered photons from a single free electron.

This mathematical formalism captures the quantum behavior of Compton scattering, emphasizing its significance at high energy scales. Compton scattering is inelastic, involving the observed recoil of charge and a transfer of energy, resulting in differences between initial and scattered photon energies.

Crucially, Compton Scattering is non-isotropic, with a higher probability of scattering for angles close to 0, as expressed mathematically through the Klein-Nishina formula.

$$\frac{d\sigma_{\text{KN}}}{d\Omega} = \frac{3}{16\pi} \sigma_T \left(\frac{\nu'}{\nu} \right)^2 \left(\frac{\nu}{\nu'} + \frac{\nu'}{\nu} - \sin^2 \theta \right)$$

$$\sigma_T = \frac{8\pi}{3} r_0^2 = \frac{8\pi}{3} \left(\frac{e^2}{m_e c^2} \right)^2 = 6.652 \times 10^{-25} \text{ cm}^2$$

where sigma T is the classical Thomson cross-section.

The total probability for a photon to be scattered by an angle theta is given by integrating the following expression.

$$\sigma_{\text{KN}} = \int_{4\pi} \frac{d\sigma_{\text{KN}}}{d\Omega}(\theta) d\Omega = \int_0^\pi \frac{d\sigma_{\text{KN}}}{d\Omega}(\theta) 2\pi \sin \theta d\theta.$$

On performing the above integration we receive the total cross-section in an analytical form given by,

$$\sigma_{\text{KN}} = \frac{3}{4}\sigma_T \left[\frac{1+x}{x^3} \left\{ \frac{2x(1+x)}{1+2x} - \ln(1+2x) \right\} + \frac{1}{2x} \ln(1+2x) - \frac{1+3x}{(1+2x)^2} \right]$$

where $x = \frac{h\nu}{mc^2}$. Further, for relativistic and classical scenarios, we obtain different versions.

2.2.1.2 Inverse Compton Scattering

When an electron and a photon collide, there is a potential for a net transfer of energy from the high-energy electron to the photon. This process is termed "inverse Compton scattering," distinguishing it from Compton scattering where lower-energy photons lose energy to electrons.

Despite involving a high-energy electron, the standard Compton scattering formula can be applied inversely, requiring a shift to a rest frame for accurate analysis. Results are then transformed back to the original frame, facilitating the determination of the scattered photon's energy or frequency.

In this context, two regimes are distinguished based on the energy of the incoming photon relative to $m_e c^2$. When the photon energy is less than $m_e c^2$, it falls into the Thomson regime. Conversely, if the photon energy exceeds $m_e c^2$, the recoil of the electron becomes significant, and the Klein-Nishina regime is applicable. In both regimes, the photon typically gains energy.

2.2.1.3 Thermal Comptonization

The phenomenon of Comptonization involves a population of cold photons undergoing spectral modification through inverse Compton scattering when encountering a region with

free electrons. The resulting change in photon energy depends on the relative energies of electrons and photons, with higher-energy electrons shifting photons to higher energies and vice versa.

When a source's spectrum is predominantly shaped by Compton processes, termed "Comptonized," the plasma must be sufficiently thin to prevent other processes, like bremsstrahlung, from dominating the spectrum. This ensures the prominence of Comptonization, and the likelihood of this process increases with hotter gas. Soft photons from the disk gain energy through multiple Compton scatterings with hot electrons, forming a corona. This process results in a power-law spectrum with a high-energy cutoff at approximately $3kT_e$ in the soft state and around kT_e in the hard state.

2.2.2 Photoelectric absorption

In X-ray spectra of sources with low energy, photoelectric absorption, also known as photoabsorption, becomes apparent. Particles within the interstellar medium, like interstellar dust or material within dense molecular clouds, absorb some X-ray photons between the source and the observer. Additionally, X-ray binaries may encounter supplementary absorption from the companion star or material in the accretion disk. This absorption process is particularly significant for photons with low energies (for $E < 1 - 10$ keV).

The accretion disk is subjected to intense X-ray radiation, particularly hard X-rays, in the proximity of the compact object. The interaction between the X-rays and the matter in the accretion disk results in a phenomenon known as reflection. One notable feature in the reflected spectrum is the emergence of the iron K line within an energy range of 6.4 to 7 keV. This iron K line serves as a crucial spectral diagnostic tool for studying the properties of matter in the innermost regions of the accretion flow around the compact object.

2.3 States of the Source

Based on the spectral properties of the X-ray-emitting components, different spectral states are identified. The two main states are,

- The **high-soft state**, characterized by the predominant thermal emission from the accretion disk and commonly observed during outbursts;

- The **low-hard state**, characterized by the prevalence of emission from the corona, is typically observed during periods of low X-ray luminosity.

2.3.1 Soft State

This state is characterized by the source being bright in soft X-rays and relatively dim in hard X-rays. The brightness in soft X-rays indicates a prevalence of lower-energy photons, while the dimness in hard X-rays suggests a scarcity of higher-energy photons.

In the high-soft state, the source spectrum is primarily characterized by a thermal component around 1 keV, linked to a geometrically thin, optically thick accretion disk. The term "geometrically thin" indicates the disk's small vertical extent relative to its radial extent.

This dominant thermal component in the spectrum can be described and modeled either by a blackbody distribution or a multi-temperature blackbody distribution. Over here, the mention of a multi-temperature blackbody suggests that the thermal emission may be coming from regions with different temperatures within the accretion disk.

The non-thermal component is described by a faint, steep power law with a photon index Γ , typically ranging from 2.1 to 3. It follows the formula $N(E) \propto E^{-\Gamma}$, where N is the number of photons and E is the photon energy (the negative exponent indicates a decrease in the number of photons with increasing energy). The non-thermal component originates from inverse Compton upscattering.

2.3.2 Hard state

In the hard state, soft X-ray luminosity is faint, and the spectrum is dominated by higher-energy X-rays. The accretion rate is relatively low compared to the soft state, with a spectral index (gamma) ranging from 1.5 to 1.9 in a hard power law. The spectrum also features a high-energy cutoff, indicating an upper limit to the emitted X-ray energy.

At lower energies, the faint thermal component indicates a cooler accretion disk, possibly truncated farther from the compact object. The suggestion of evaporation affecting the

inner disk remains a hypothesis.

In this state, the accretion disk interacts with a larger, cooler corona of hot electrons, resulting in a dominant corona-shaped X-ray spectrum. The absence of the innermost disk leads to weaker reflection features compared to the soft state.

Chapter 3

X-Ray Astronomy

X-ray astrophysics, emerging in the 1960s, changed how we see the universe by looking beyond Earth's atmosphere. X-rays (0.1 to 100 keV) help us study high-energy events like black holes. X-ray detectors count individual photons, posing statistical challenges. Soft and hard X-rays show low and high energy.

Analyzing X-ray events helps astronomers understand cosmic sources. This field contributes to our knowledge of extreme space environments, often combined with multiwave-length studies. Ongoing advances in space observatories and detectors continue to reveal insights into the universe's energetic processes.

The Earth's atmosphere shields against X-rays through photoelectric absorption, safeguarding life by blocking harmful cosmic radiation. X-ray observatories are launched into space for unimpeded observations due to this atmospheric opacity.

3.1 Missions based on X-Ray Astronomy

The history of X-ray astronomy traces its origins to the post-World War II era, with a military context driving its early development. The initial exploration involved rocket flights above the atmosphere to study X-ray emissions from the solar corona.

In 1962, R. Giacconi and his team identified Scorpius X-1, a bright non-solar X-ray source, leading to Giacconi's Nobel Prize in 2002 for his contributions. Advancements in detectors, particularly spatial resolution improvements, revealed Scorpius X-1 as a binary system with a neutron star. Subsequent satellites further explored the X-ray regime.

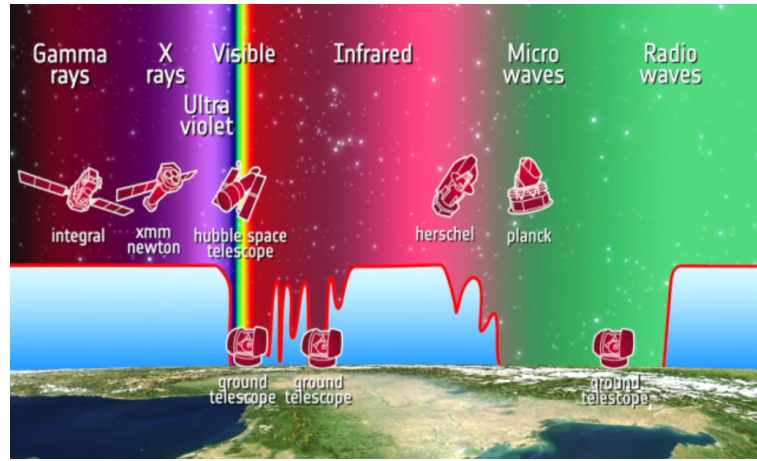


Figure 3.1: Electromagnetic Waves absorption in atmosphere

The below table would have given you a good idea about the X-ray missions that have taken place till now. The current era represents a "Golden Age" for X-ray astronomy, marking the first time that numerous X-ray missions are simultaneously conducting observations. This period is characterized by a suite of advanced observatories, including XMM-Newton, Chandra, INTEGRAL, MAXI, Swift, Suzaku, and the recent addition of NuSTAR.

Together, these missions offer a unique combination of key capabilities:

- High angular resolution
- Large effective area for enhanced sensitivity
- Large effective area for enhanced sensitivity
- Agility for flexible pointing
- Agility for flexible pointing
- High-resolution spectroscopy for detailed spectral analysis
- The ability to observe across a broad energy spectrum from soft to hard X-rays
- Continuous monitoring of sources
- Dedicated observation of hard X-rays

This collective suite covers an exceptionally vast energy range, enabling comprehensive studies of various celestial phenomena across different wavelengths, from stars and galaxies to active galactic nuclei.

Name	Operation years	Bandpass (keV)	Main Space Agency
Uhuru	1970 – 1973	1.7 – 18	NASA
ANS	1974 – 1976	0.2 – 30	NISR/NASA
Ariel-V	1974 – 1980	0.9 – 1 200	SRC/NASA
SAS-3	1975 – 1979	0.1 – 60	NASA
OSO-8	1975 – 1978	0.15 – 1 000	NASA
HEAO-1	1977 – 1979	0.15 – 10 000	NASA
Einstein	1978 – 1981	0.15 – 20	NASA
Hakucho	1979 – 1985	0.1 – 100	ISAS
Tenma	1983 – 1985	0.1 – 100	ISAS
EXOSAT	1983 – 1986	0.05 – 50	ESA
GINGA	1987 – 1991	1.5 – 500	ISAS
Granat	1989 – 1998	2 – 100 000	RSA
ROSAT	1990 – 1999	0.1 – 2.4	GAC/NASA
ASCA	1993 – 2000	0.4 – 10	ISAS
BeppoSAX	1996 – 2002	0.1 – 300	ASI/NIVR
RXTE	1995 – 2012	2 – 250	NASA
Chandra	1999–	0.06 – 10	NASA
XMM-Newton	1999–	0.15 – 15	ESA
INTEGRAL	2002–	4 – 10 000	ESA
Swift	2004–	0.2 – 150	NASA
Suzaku	2005–	0.2 – 600	JAXA/NASA
MAXI	2009–	0.5 – 30	JAXA
NuSTAR	2012–	5 – 80	NASA

Figure 3.2: X-Ray missions

The majority of the current X-ray astronomy missions are outfitted with X-ray Charge-Coupled Devices (CCDs). These detectors offer a significantly enhanced spectral resolution compared to proportional counters, a different type of X-ray detector.

In this report, I will be mostly talking about the NuSTAR mission and the data collected by it.

3.2 NuSTAR Mission

The Nuclear Spectroscopic Telescope Array (NuSTAR) is a space-based X-ray telescope designed to observe high-energy X-rays, focusing on the hard X-ray portion of the electromagnetic spectrum. NuSTAR was developed by NASA and launched on June 13, 2012, as a Small Explorer mission. It represents a significant advancement in X-ray astronomy due to its capability to observe in the energy range of 3 to 79 keV, which is higher than the range covered by previous X-ray telescopes.

Below list the key features of this mission:

- **High Energy Sensitivity**

Sensitive to high-energy X-rays, allowing it to investigate astrophysical phenomena such as active galactic nuclei (AGN), supernova remnants, and compact objects like black holes and neutron stars.

- **Focusing Optics**

Employs a focusing optics design, utilizing nested, grazing-incidence X-ray mirrors. This design enhances the telescope's ability to focus high-energy X-rays, providing better spatial resolution compared to previous missions in the hard X-ray regime.

- **Detectors:**

Equipped with state-of-the-art cadmium-zinc-telluride (CZT) pixel detectors, which are sensitive to X-rays in the hard energy range. These detectors contribute to NuSTAR's improved sensitivity and spatial resolution.

- **Observations of Black Holes and Neutron Stars**

One of the mission's primary goals is to study the energetic processes near black holes and neutron stars. By observing in the hard X-ray band, NuSTAR can penetrate

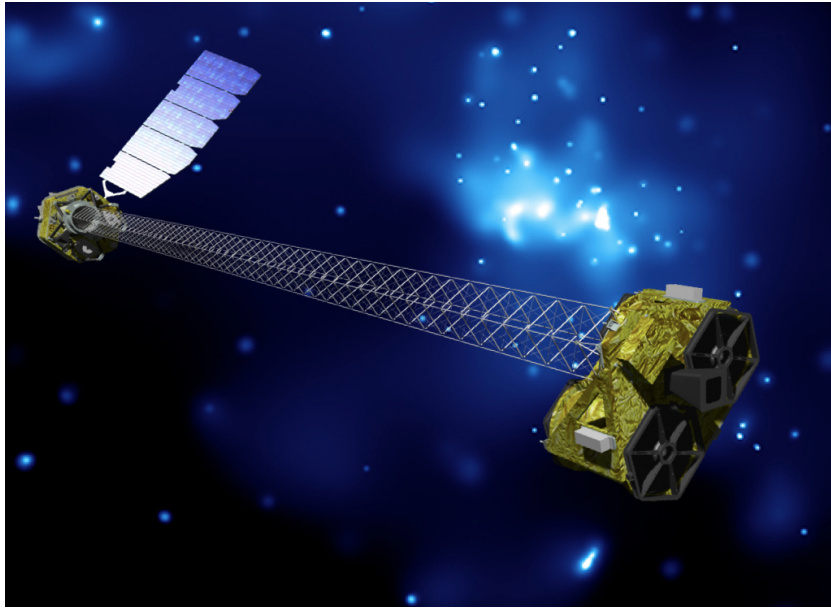


Figure 3.3: NuSTAR satellite

the dense environments around these objects and provide insights into the physics of accretion and high-energy particle acceleration.

- **Surveys of the Galactic Plane**

Used to conduct surveys of the Galactic Plane, studying the distribution and characteristics of X-ray sources in our Milky Way galaxy.

- **Complementary to Other Observatories**

Often used in conjunction with other space-based observatories, such as Chandra and XMM-Newton, to provide a more comprehensive understanding of celestial objects across different wavelengths.

3.2.1 Major Scientific Discoveries

- **First Measurement of the Black-hole spin with high precision**

The spin rate of the supermassive black hole at the core of the NGC 1365 galaxy was measured by NuSTAR and XMM-Newton in February 2013.

The technique of analyzing the frequency change of X-ray light provided valuable insights into the dynamics of material near supermassive black holes, enhancing our understanding of these enigmatic cosmic objects.

- **Untangling the mystery of how stars explode:**

One of NuSTAR's primary objectives is to characterize stellar explosions by mapping the distribution of radioactive material in supernova remnants.

In computer simulations of supernova explosions, the main shock wave frequently stalls as a massive star undergoes collapse. In many cases, the star fails to undergo complete disruption.

- **Discovery of a shockingly bright dead star:**

On April 6th, 2023, the NuSTAR team made a significant observation regarding the neutron star M82 X-2. They confirmed that this neutron star was emitting a higher amount of radiation than what was previously considered physically possible based on the Eddington limit.

- **Staring deep into the hidden lairs of the Black Hole:**

The identification of supermassive black holes at the nuclei of nearby galaxies NGC 1448 and IC 3639 has been unveiled through the analysis of NuSTAR data.

- **Contributed to the first picture of the black hole:**

In a groundbreaking discovery, the NuSTAR and XMM-Newton telescopes detected X-ray radiation from behind a supermassive black hole in the Seyfert 1 galaxy I Zwicky 1. Stanford University researchers observed that light from an initial flash reflected off the black hole's accretion disk, causing delayed and frequency-shifted signals at the detector. The curved spacetime around the black hole redirected the reflected light toward the detector after the initial flash.

Chapter 4

Data Analysis

4.1 A little background on XSPEC

XSPEC is specialized software created for analyzing and modeling X-ray spectra in astrophysics. It was developed by HEASARC which stands for High Energy Astrophysics Science Archive Research Center, belonging to NASA. XSPEC is extensively used by astronomers and astrophysicists to examine data from X-ray observatories like XMM-Newton, Chandra and Suzaku.

- **Spectral Modeling:**

Provides a platform for modeling and fitting X-ray spectra. Researchers can use various mathematical models to describe the emission processes occurring in astrophysical sources, such as thermal emission from hot plasmas, power-law components, and absorption features.

- **Statistical Analysis:**

The software uses statistical methods to fit models to observed data, allowing researchers to assess the goodness of fit and obtain parameters for their chosen models. Common statistical methods include (chi-squared) minimization.

- **Instrument Response:**

It accounts for the instrumental response of X-ray detectors, which is crucial for accurately interpreting observational data. It allows researchers to tune their models with the response functions of specific X-ray instruments.

- **Interactive Graphical Interface:**

Provides an interactive graphical interface that allows users to visualize their data,



Figure 4.1: XSPEC LOGO

models, and fit results. This makes it user-friendly and accessible to scientists with varying levels of expertise.

- **Extensibility:**

Users can customize and extend XSPEC by adding their own models or fitting functions, making it a flexible tool for a wide range of astrophysical analyses.

- **Community Support:**

XSPEC has an active user community, and the software is regularly updated with improvements and bug fixes. Documentation and user support are available to assist researchers in using the software effectively.

4.2 Basics of Spectral fitting

The observed spectrum, represented by photon counts() within specific instrument channels (I) is related to the actual spectrum of the source ($f(E)$) by the equation.

$$C(I) = \int f(E)R(I, E)dE$$

In this equation,

- $C(I)$: Observed spectrum (photon counts) in channel I
- $f(E)$: Actual spectrum of the source as a function of energy (E)
- $R(I, E)$ represents the instrumental response, indicating the likelihood that a photon with energy E will be detected in channel I .

However, attempting to invert this equation to deduce the actual spectrum ($f(E)$) from a given set of observed counts ($C(I)$) is typically impractical due to the non-uniqueness and instability caused by small changes in $C(I)$. Instead, the common approach involves selecting a model spectrum ($f(E, p1, p2, \dots)$) with a few parameters and fitting it to the observed data.

For every model spectrum, a predicted count spectrum ($C_p(I)$) is computed and contrasted with the observed data ($C(I)$). A "fit statistic" is then calculated from this comparison to evaluate the model spectrum's compatibility with the data collected by the spectrometer. In this fitting process, the model parameters are adjusted to enhance the alignment between the predicted and observed spectra.

The prevalent fit statistic used to identify the "best-fit" model is the chi-squared (χ^2), defined by the following formula,

$$\chi^2 = \sum (D_i - M_i)^2 / \sigma_i^2$$

Once we obtain a best fit, we should ask ourselves the following two questions,

- The adequacy of a model, measuring the alignment of observed data with the best-fit model, is assessed using the χ^2 statistic. Computed as the sum of squared differences normalized by uncertainties, χ^2 is compared to a critical value corresponding to a selected confidence level, considering degrees of freedom (μ) that account for the difference between channels and model parameters.

A reduced χ^2 close to 1 indicates a good fit, but exceeding this suggests a poor fit, and falling below indicates potential overestimated errors. Passing the goodness-of-fit test doesn't establish model uniqueness; alternative models may also provide acceptable fits, highlighting the need for cautious interpretation even when a model is deemed adequate.

- The confidence interval for a given best-fit parameter ($p1$) represents the range of values wherein one can confidently assert that the true parameter value exists. This interval is determined by adjusting the parameter value until the χ^2 statistic increases by a specific amount above the minimum (best-fit) value. The increment in χ^2 is known as the critical $\Delta\chi^2$, and it depends on the chosen confidence level and the

number of parameters considered in the calculation.

A higher critical $\Delta\chi^2$ corresponds to a broader confidence interval, allowing for a greater range of parameter values consistent with the observed data. The confidence interval provides a statistical measure of the uncertainty associated with the best-fit parameter estimate.

4.3 Implementation

So the procedure in XSPEC can be summarised into the following commands,

- **Choose a Parameterized Model:**

In XSPEC, researchers typically choose a parameterized model from a library of available models. Examples include power-law models, thermal bremsstrahlung, and more complex models like absorbed power laws or emission lines.

- **Choose Initial Parameter Values:**

Assign initial values to the parameters of the chosen model. These initial values serve as starting points for the fitting procedure.

- **Predict Count Spectrum:**

XSPEC utilizes the selected model and parameter values to forecast the count spectrum that would be observed by the X-ray spectrometer.

- **Compare Predicted Spectrum to Observed Data:**

Compare the forecasted spectrum with the real spectrum acquired by the X-ray instrument. XSPEC offers tools for visualizing and examining this comparison.

- **Manipulate Parameters for Best Fit:**

Leverage the fitting capabilities of XSPEC to methodically fine-tune the model parameters until the optimal match between the theoretical model and the observed data is attained. This process commonly entails minimizing the χ^2 statistic.

- **Calculate Goodness-of-Fit:**

XSPEC calculates the goodness-of-fit using the χ^2 statistic. The lower the χ^2 , the better the fit. XSPEC also provides statistical measures such as the reduced χ^2 .

- **Calculate Confidence Intervals:**

After obtaining the best-fit parameters, XSPEC can calculate confidence intervals for each parameter. This is done by varying each parameter individually and finding the range of values that are consistent with the observed data within a certain confidence level.

- **Model Assessment:**

Interpret the results, considering the goodness-of-fit and confidence intervals. A low χ^2 and narrow confidence intervals indicate a robust fit.

- **Iterative Refinement:**

If needed, iterate through the process, refining the model and parameter values based on the goodness-of-fit and confidence interval assessments.

This gives the basic framework for implementing the software.

4.4 Some Basic Commands

- **Loading Data:**

Load your X-ray spectrum data into XSPEC. This typically involves reading in a data file containing the observed counts and associated response and background files.

```
XSPEC> data <filename>
XSPEC> response <responsefilename>
XSPEC> backgrnd <backgroundddfilename>
```

You can simultaneously load files at the same time as well.

```
XSPEC> data 1:1 nameoffile1 2:2 nameoffile2
```

- **Model Definition:**

Choose a model that represents the physical processes you expect to be occurring in the source. XSPEC provides a variety of predefined models. For example, to use a power-law model:

```
XSPEC> model powerlaw
XSPEC> model diskbb
```

```
XSPEC> model tbabs(diskbb + powerlaw)
```

We can use a combination of models to model our spectrum.

- **Setting Parameters:**

Set the initial values for the model parameters. You may need to adjust these parameters to best fit your data.

```
XSPEC> par 1 1.0 (Set the first parameter of the model to 1.0)
```

Parameters can be made freezable as per your needs. To do that, we type the following command.

```
XSPEC> new 1 1.5 -1
```

One can even unfreeze the parameter value, in the process if required. This can be done by,

```
XSPEC> thaw 1
```

If the parameter values are not entered when asked by the software, it will presume its default value for those parameters.

- **Fitting:**

Fit the model to the data. This minimizes the difference between the observed data and the model prediction.

```
XSPEC> fit
```

- **Viewing Results:**

After fitting, you can view various results, including parameter values, fit statistics, and plots.

```
XSPEC> setplot energy (Changes from channel to energy)
```

```
XSPEC> ignore 1: **-3.0 7.0-** (ignores the energy range from 3 to 7 keV) XSPEC>
show parameters (Display parameter values)
```

```
XSPEC> show fit (Display fit statistics)
XSPEC> plot data (Plot the data)
XSPEC> plot model (Plot the model)
XSPEC> pl uf del
XSPEC> pl uf ratio
```

- **Saving Results:** Save the fit results and plots for further analysis or reporting.

```
XSPEC> save all <outputfilename>
```

Your file will be saved as a .xcm file. You can open the same file by doing the following.

```
XSPEC> open <outputfilename>
```

- **Error:**

The error command in XSPEC is used to compute the error of various parameters.

```
XSPEC12> error 1-4 (Estimate the 90percent confidence ranges for each parameter.)
```

```
XSPEC12> error 2.706 1 3 1. 2(Estimate the 90percent ranges for parameters 1 and 3 and the 1. sigma)
```

The error can be calculated namely in two ways. The first is the MCMC method and the second is the normal error method. For my internship, I have used the MCMC method.

- **Exiting XSPEC:** When you are done, you can exit XSPEC.

```
XSPEC> exit
```

Chapter 5

Studying 4U 1543-47 outbursts

5.1 Introduction

The object 4U 1543-47 is an X-ray binary system. The designation "4U" indicates that this source was cataloged as part of the fourth Uhuru catalog of X-ray sources, which was a pioneering satellite-based X-ray observatory launched in the 1970s. Its status as a black hole binary had not been confirmed until 1984 by astronomer S. Kiamoto and colleagues.

The coordinates for 4U 1543-47 are approximately,

Right ascension: 15h 47m 08s

Declination: -47° 40' 12"

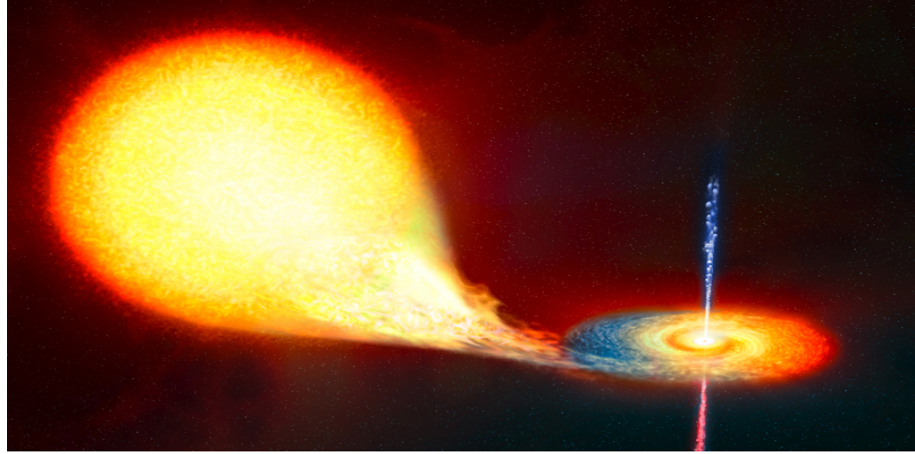
During the analysis, there were 10 publicly available observations of the X-ray binary system 4U 1543-47, identified by the following observation IDs: **80702317002, 80702317004, 80702317006, 80702317008, 90702326002, 90702326004, 90702326006, 90702326008, 90702326010, and 90702326012.**

All of these observations were conducted during the 2021 outburst. The source flux diminishes with each successive observation.

Here, we assume a mass of $M = 9.4 \pm 2 M_{\odot}$ and a distance of $d = 7.5 \pm 1$ kpc. The observations are captured when the source is at an Eddington fraction greater than 0.3.

This analysis involves considering a range of possible black hole masses and distances to the system. In the last four observations, the Eddington fraction, indicating the system's radiation properties, varies between approximately 0.32 and 0.8. Concerns arise regarding

the accuracy of parameter estimates(which will be discussed further), particularly in the first observation, where an unusually high Eddington fraction suggests potential inaccuracies in mass and distance estimates. To address this, the analysis allows for variations in the inner disk radius during spectral fitting.

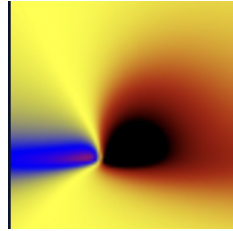


The above is an artistic impression of the 4U 1543-47 X-Ray Binary system.

The spectra are fitted over the NuSTAR bandpass of 3–79 keV for all observations, offering a comprehensive study of X-ray emissions.

5.2 Relxill Component

The **relxill** model is specifically employed for investigating relativistic effects in the vicinity of black holes, such as the reflection of X-rays off the accretion disk. It considers the relativistic blurring and gravitational redshift occurring near massive objects like black holes.



It represents an enhanced version that integrates components from the **xillver** reflection code and the **relline** ray-tracing code. A notable feature of **relxill** is its capability to select the appropriate xillver-reflection spectrum for each point on the accretion disk, determined by relativistically calculated emission angles.

Regarded as a more consistent and physically accurate representation, this model exhibits enhanced precision compared to its predecessors. The **relxill** model demonstrates improved accuracy in determining both the inclination and the spin parameter of black holes at a 90% confidence level, outperforming older, angle-averaged models at a 69% confidence level.

The introduction of this model underscores its importance in interpreting observational data from accreting sources, particularly in anticipation of analyzing higher-quality data from new observatories such as NuSTAR and Astro-H.

The "relxill" model is considered a significant step toward a more physical and self-consistent representation of X-ray reflection from accretion disks around black holes.

- **'xillver' Reflection Code:**

xillver is a code that models X-ray reflection off an accretion disk around a black hole. It considers the effects of Compton scattering, photoelectric absorption, and fluorescence emission.

The relxill model enhances this by dynamically choosing the appropriate xillver spectrum for each point on the accretion disk.

- **'relline' Ray-Tracing Code:**

relline is a ray-tracing code that calculates the relativistic effects near a black hole, such as gravitational redshift and light bending.

By combining **xillver** with **relline**, relxill incorporates relativistic corrections into the reflection model.

- **Proper Spectrum Selection:**

For each point on the accretion disk, relxill selects the proper xillver-reflection spectrum based on relativistically calculated emission angles. This ensures a more accurate representation of the reflection process in the strong gravitational field near a black hole.

For my internship I have used relxill v.1.4.3, which I have installed from the website itself. In addition to this, the makers Dausier and Garcia have introduced flavours in the model, such as **relxilllpCp**, **relxilllp** etc.

A last thing to add is that the relxill model has to be explicitly loaded in XSPEC using the load command.

```
XSPEC> load relxill <file location>
```

5.3 Markov Chain Monte Carlo (MCMC)

In X-ray spectral analysis, Markov Chain Monte Carlo (MCMC) is a technique used to explore the parameter space of a model and estimate uncertainties on the model parameters. This is particularly useful when dealing with complex models and when you want a robust estimation of uncertainties.

The MCMC chain in XSPEC refers to the sequence of model parameter values generated during the MCMC analysis. Here's a brief overview of how the MCMC chain works in XSPEC:

- **Initialization:**

The MCMC chain starts with an initial set of model parameter values. These values are typically chosen randomly, or they may be based on a previous analysis.

- **Proposal Distribution:**

At each step of the chain, a proposal distribution is used to suggest a new set of parameter values. The proposal distribution defines how the parameters should be adjusted from their current values.

- **Acceptance/Rejection:**

The proposed parameter values are then either accepted or rejected based on the likelihood of the data given the model. If the proposed values improve the fit to the data, they are more likely to be accepted. If not, there's still a chance they could be accepted to explore the parameter space thoroughly.

- **Chain Evolution:**

The process of proposing, accepting/rejecting, and updating parameter values is repeated for a large number of iterations. This allows the chain to explore the entire parameter space and converge toward the regions of highest likelihood.

- **Burn-in:**

The initial part of the MCMC chain, where the algorithm is still converging to the

optimal region, is often discarded. This is known as the "burn-in" period.

- **Parameter Estimates:**

The final set of parameter values obtained from the MCMC chain provides estimates for the model parameters, and the dispersion of these values gives an indication of the uncertainties associated with each parameter.

The commands in XSPEC for implementing the MCMC chain are as follows,

XSPEC12> chain type gw (**setting the chain type, we will use greenwood here, which is chosen by default**)

XSPEC12> chain walkers 8(**how many CPU cores you're going to use**)

XSPEC12> parallel walkers 4(**number of CPU cores it will use parallelly**)

XSPEC12> chain length 1000 (**length of the chain**)

XSPEC12>chain run test1.fits (**this is where the chain creation process starts, and it might take a while, depending on the number of CPU cores has**)

XSPEC12>plot chain 0 (**look at the distribution**)

XSPEC12> chain burn 100 (**remove 1st 100 points**)

XSPEC12>error 1 (**will compute the error in parameter 1, like mentioned above**)

The best-fit parameter combination obtained from the baseline models serves as the initial point for the MCMC walkers. Uniform priors are applied within the allowable parameter ranges, and the Xspec emcee implementation is employed for the MCMC analysis. A substantial number of walkers, on the order of several times the number of free parameters, is chosen to ensure a thorough exploration of the parameter space.

That concludes our discussion on MCMC analysis relevant to our topic.

5.4 Models and Parameters used for this source

Now I will talk about the models and parameters that I have used for modelling the spectrum of this source. I have done the fitting process several times to obtain the best possible fit with a chi-squared value close to one and suitable parameters. The process involved changing the parameter values, freezing, thawing, and re-fitting. It is a long repetitive task that requires consistency and patience.

I have used the following models for the data analysis of this source.

- **Tbabs:**

Enables users to adjust solely the hydrogen column, functioning as a multiplicative model. It involves a single parameter, namely,

$$nH = \text{equivalent hydrogen column (in units of } 10^{22} \text{ atoms cm}^{-2})$$

- **zxipcf:**

This model employs a grid of XSTAR photoionized absorption models for absorption, presuming that this process only accounts for a fraction f of the source. The remaining $(1-f)$ of the spectrum is assumed to be directly observed.

It has the following parameters,

No.	Notation	Definition
par 1	Nh	column density 10^{22} cm^2
par 2	log_xi	$\log(\xi)$ where $\xi=L/nr^2$
par 3	CvrFrac	covering fraction
par 4	Redshift	redshift

- **diskbb:**

The spectrum from an accretion disk consists of multiple blackbody components and is modeled using the diskbb model.

It has the following parameters,

No.	Notation	Definition
par 1	Tin	temperature at inner disk radius (keV)
par 2	norm	will write it

- **relxill:**

Well, I have talked about the relxill component before. Now I will talk more about its parameters. array margin=1in

No.	Notation	Definition
par 1	Index1	used in defining emissivity
par 2	Index2	used in defining emissivity
par 3	Rbr	break radius
par 4	a	The spin of the black hole is expressed in dimensionless units, where negative values indicate that the accretion disk is counter-rotating relative to the black hole.
par 5	Incl	The inclination is defined as the angle towards the system concerning the normal to the accretion disk.
par 6	Rin	The inner radius of the accretion disk is expressed in gravitational radii.
par 7	Rout	The outer radius of the accretion disk is specified in gravitational radii.
par 8	z	redshift to the source
par 9	gamma	Power law index of the incident spectrum.
par 10	logxi	The ionization state of the accretion disk ranges from 0 (neutral) to 4.7 (heavily ionized).
par 11	Afe	The iron abundance of the material in the accretion disk
par 12	Ecut	The parameter describing the observed high-energy cutoff, denoted as E_{cut} , characterizes the primary spectrum.
par 13	refl_frac	The ratio of intensity emitted towards the disk compared to escaping to infinity is referred to as the emission intensity ratio.
par 14	norm	normalization parameter

This gives us a basic description of what the parameters signify.

5.5 Observations

Since we now have a better understanding of the models and the parameters, we will dive into the spectral analysis of the 4U 1543-47 observations recorded by the NuSTAR mission. There were a total of 10 observations that were recorded from the source over a span of several days.

Initially, my guide had made me model the spectrum excluding the `relxill` component, using other models such as `gabs`, `lorentz`, and `gaussian`. The sole purpose was to understand the difference in the usage of models and for the sake of practice as well. It also gave me a chance to explore other models.

For each observation, I have used the following combination of models,

```
XSPEC> model tbabs*zxipcf*(diskkbb + relxill)
```

After this, I had to enter the parameter values for each model. I was using the reference for the values from a research paper **A Systematic View of Ten New Black Hole Spins by Paul A. Draghis**. They computed the parameter values for the four observations(90702326006, 90702326008, 90702326010, and 90702326012) which were of great help to me. For the remaining observations, I had to find the parameter values on my own.

The parameter values I obtained were comparable with the values given in the paper. The difference is because of different compilers and software environments.

5.5.1 80702317002

For this observation, below are the parameter values that I obtained after getting the best fit. After multiple multiple fittings of days and nights, I have received this fit. Some parameter values are frozen such as Redshift, Rout, and z. This is done because we neglect the redshift in this observation and Rout is made fixed otherwise this parameter starts jumping up and down during the fitting process thus harming the other parameter values. One other thing to notice is that the values of the norm of **diskbb** and **relxill** for Data Group 2 are not equal to those to of Data Group 1.

The Index2 parameter was frozen because it doesn't vary during the fitting process at all. Instead, it also shows this message,

*****Warning: Zero alpha-matrix diagonal elements for parameter 9. Parameter 9 is pegged at 2e-07 due to zero or negative pivot element, likely caused by the fit being insensitive to the parameter.**

This reason is applied to other observations as well, where this particular parameter is frozen.

Below is the plot for the best-fit curve. After this, I had to compute the errors for each parameter for which I used the MCMC analysis. The chain length for which I could run it went to a maximum of 500000 beyond which the computer couldn't produce better results. The burn-in was set to 50000. This chain length varies for each observation. On computing the errors I get the following values.

```

Data group: 1
 1  1  TBabs      nH      10^22    0.480052    +/-  0.357311
 2  2  zxipcf     Nh      10^22    28.3931    +/-  8.76716
 3  2  zxipcf     log_xi   1.89368   +/-  0.351117
 4  2  zxipcf     CvrFract 0.210575   +/-  6.46291E-02
 5  2  zxipcf     Redshift 0.0       frozen
 6  3  diskbb     Tin      keV     1.16540   +/-  1.27933E-02
 7  3  diskbb     norm    1.08766E+04 +/-  1371.84
 8  4  relxill    Index1  5.75399   +/-  1.53123
 9  4  relxill    Index2  2.00000E-07 frozen
10  4  relxill    Rbr     20.0000   +/-  12.3105
11  4  relxill    a       0.978855  +/-  3.46627E-02
12  4  relxill    Incl    deg     65.8540   +/-  2.18461
13  4  relxill    Rin     -1.00000  +/-  0.158179
14  4  relxill    Rout    400.000   frozen
15  4  relxill    z       0.0       frozen
16  4  relxill    gamma   3.38704  +/-  0.288888
17  4  relxill    logxi   2.99016  +/-  1.05396
18  4  relxill    Afe    10.0000   +/-  11.5977
19  4  relxill    Ecut    keV     91.0877   +/-  108.265
20  4  relxill    refl_frac 3.66885  +/-  2.84825
21  4  relxill    norm   2.70118   +/-  1.57792

Data group: 2
22  1  TBabs      nH      10^22    0.480052    = p1
23  2  zxipcf     Nh      10^22    28.3931    = p2
24  2  zxipcf     log_xi   1.89368   = p3
25  2  zxipcf     CvrFract 0.210575   = p4
26  2  zxipcf     Redshift 0.0       = p5
27  3  diskbb     Tin      keV     1.16540   = p6
28  3  diskbb     norm   1.02132E+04 +/-  1292.95
29  4  relxill    Index1  5.75399   = p8
30  4  relxill    Index2  2.00000E-07 = p9
31  4  relxill    Rbr     20.0000   = p10
32  4  relxill    a       0.978855  = p11
33  4  relxill    Incl    deg     65.8540   = p12
34  4  relxill    Rin     -1.00000  = p13
35  4  relxill    Rout    400.000   = p14
36  4  relxill    z       0.0       = p15
37  4  relxill    gamma   3.38704  = p16
38  4  relxill    logxi   2.99016  = p17
39  4  relxill    Afe    10.0000   = p18
40  4  relxill    Ecut    keV     91.0877   = p19
41  4  relxill    refl_frac 3.66885  = p20
42  4  relxill    norm   2.62878   +/-  1.53735

-----
Fit statistic : Chi-Squared =          558.59 using 401 PHA bins.
***Warning: Chi-square may not be valid due to bins with zero variance
           in spectrum number(s): 2

```

Figure 5.1: Parameters of 80702317002

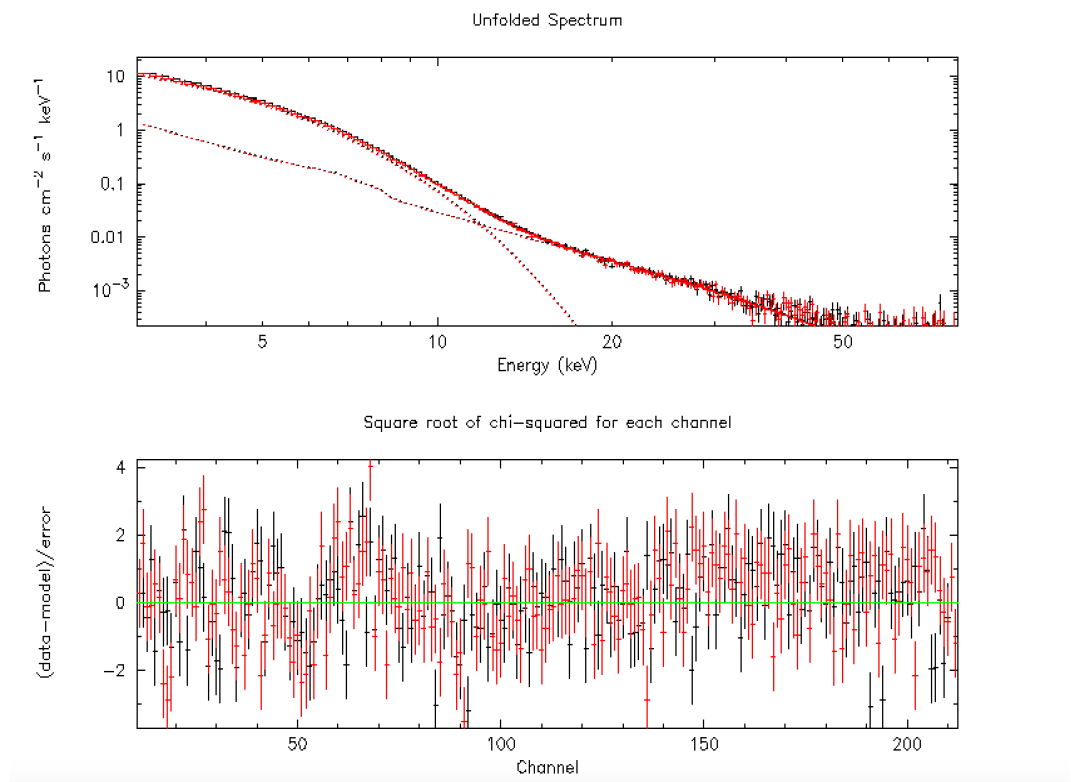


Figure 5.2: Plot of 80702317002

5.5.2 80702317004

For this observation, below are the parameter values that I obtained after getting the best fit. Few parameters in this fit are subjected to the same freezing conditions as before. Below is the modeled spectrum plot that I have obtained. Above are the error values with respect to their 1-sigma confidence intervals. The chain length was set to 100000 with a burn-in of 10000.

5.5.3 80702317006

Below are the produced parameters for the best fit obtained. The reduced chi-squared ratio is not very close to one, but it is the best fit I have obtained. Next, I will show a plot of the modeled spectrum. Above is an image of the error values with their intervals for each parameter. This was a time-consuming task as it had to be re-fit again and again for accurate results. The chain length was set to 115000 with a burn-in phase of 10000. The chain length is smaller compared to the ones in the other observations because the software was misbehaving for higher chain number values. It showed errors like "Broken Pipe".

5.5.4 80702317008

Below are the produced parameters for the best fit obtained. The chi-squared value is not very close to 1 but it was the best I could have obtained in the given time frame. Now I will display the modeled spectrum below. This was done using the,

XSPEC> pl uf del The above figure will give us an idea of the error analysis of each parameter using MCMC with their respective confidence intervals.

5.5.5 90702326002

Below are the produced parameters for the best fit obtained. The modeled spectrum.

Data group: 1							
1	1	TBabs	nH	10^{22}	0.726493	+/-	0.253988
2	2	zxipcf	Nh	10^{22}	44.5744	+/-	3.19446
3	2	zxipcf	log_xi		1.90861	+/-	5.75048E-02
4	2	zxipcf	CvrFract		0.395225	+/-	1.08263E-02
5	2	zxipcf	Redshift		0.0	frozen	
6	3	diskbb	Tin	keV	1.01676	+/-	3.49819E-03
7	3	diskbb	norm		1.79714E+04	+/-	484.704
8	4	relxill	Index1		10.0000	+/-	8.32486
9	4	relxill	Index2		2.00000E-07	frozen	
10	4	relxill	Rbr		24.9680	+/-	93.2970
11	4	relxill	a		0.938548	+/-	6.60397E-02
12	4	relxill	Incl	deg	69.5422	+/-	2.47553
13	4	relxill	Rin		-1.05988	+/-	0.220828
14	4	relxill	Rout		400.000	frozen	
15	4	relxill	z		0.0	frozen	
16	4	relxill	gamma		3.40000	+/-	0.647348
17	4	relxill	logxi		2.70258	+/-	1.19459
18	4	relxill	Afe		10.0000	+/-	11.3129
19	4	relxill	Ecut	keV	1000.00	+/-	2.45939E+04
20	4	relxill	refl_frac		3.32117	+/-	5.96643
21	4	relxill	norm		1.06779	+/-	1.29020
Data group: 2							
22	1	TBabs	nH	10^{22}	0.726493	= p1	
23	2	zxipcf	Nh	10^{22}	44.5744	= p2	
24	2	zxipcf	log_xi		1.90861	= p3	
25	2	zxipcf	CvrFract		0.395225	= p4	
26	2	zxipcf	Redshift		0.0	= p5	
27	3	diskbb	Tin	keV	1.01676	= p6	
28	3	diskbb	norm		1.70749E+04	+/-	462.385
29	4	relxill	Index1		10.0000	= p8	
30	4	relxill	Index2		2.00000E-07	= p9	
31	4	relxill	Rbr		24.9680	= p10	
32	4	relxill	a		0.938548	= p11	
33	4	relxill	Incl	deg	69.5422	= p12	
34	4	relxill	Rin		-1.05988	= p13	
35	4	relxill	Rout		400.000	= p14	
36	4	relxill	z		0.0	= p15	
37	4	relxill	gamma		3.40000	= p16	
38	4	relxill	logxi		2.70258	= p17	
39	4	relxill	Afe		10.0000	= p18	
40	4	relxill	Ecut	keV	1000.00	= p19	
41	4	relxill	refl_frac		3.32117	= p20	
42	4	relxill	norm		1.04565	+/-	1.26320

Fit statistic : Chi-Squared = 515.99 using 409 PHA bins.

Figure 5.3: Parameters of 80702317004

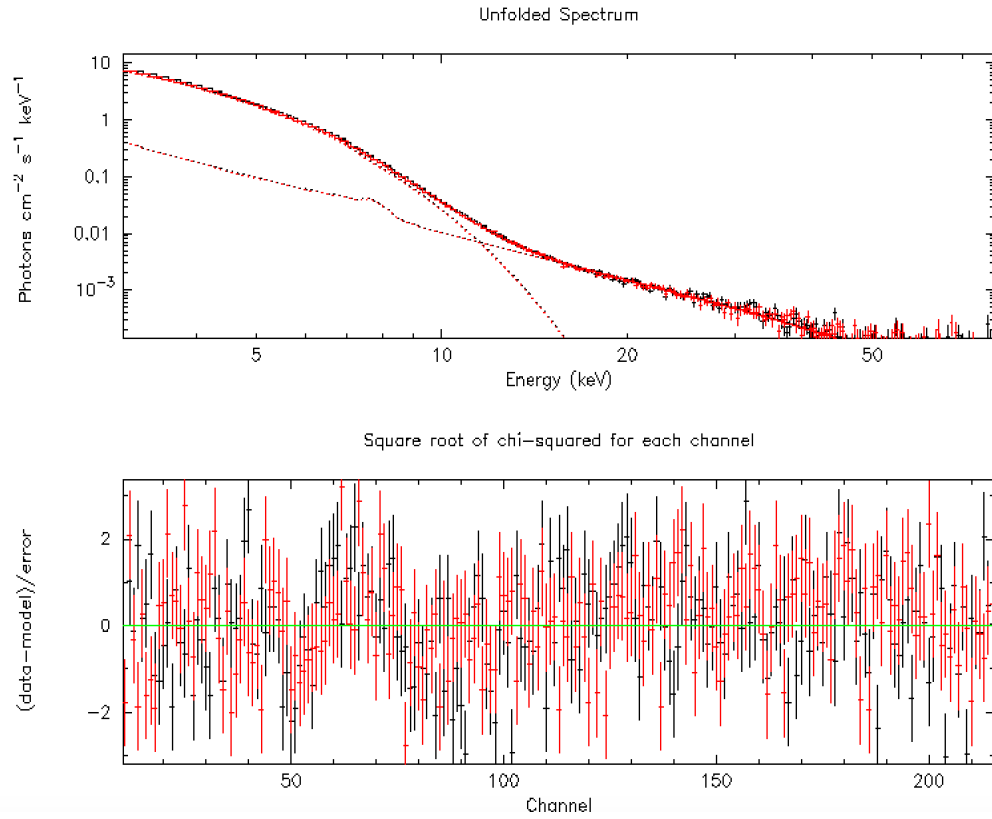


Figure 5.4: Plot of 80702317004

Parameter	Confidence Range (1)
1	0.722814 0.726623 (-0.00367891, 0.000130041)
2	44.448 44.5843 (-0.126368, 0.00989774)
3	1.9039 1.90991 (-0.00471222, 0.00129385)
4	0.395052 0.395861 (-0.000172564, 0.000636107)
6	1.01665 1.01696 (-0.000106954, 0.00020192)
7	17949.6 17982.9 (-21.8195, 11.4892)
8	10 10 (0, 0)
10	24.9639 25.0501 (-0.00402968, 0.0821237)
11	0.937677 0.940634 (-0.000870838, 0.00208587)
12	69.403 69.669 (-0.139232, 0.126811)
13	-1.06258 -1.05975 (-0.00270288, 0.000124354)
16	3.39895 3.4 (-0.00105152, 0)
17	2.70188 2.7131 (-0.000697459, 0.0105285)
18	10 10 (0, 0)
19	996.739 1000 (-3.2614, -1.13687e-12)
20	3.3168 3.32536 (-0.00436668, 0.00419278)
21	1.06334 1.06798 (-0.00445065, 0.00019224)
28	17051 17093.6 (-23.8997, 18.686)
42	1.03815 1.04639 (-0.00749488, 0.000743541)

Figure 5.5: Errors of 80702317004

Data group: 1							
1	1	TBabs	nH	10^22	0.217273	+/-	0.225402
2	2	zxipcf	Nh	10^22	38.8523	+/-	2.41573
3	2	zxipcf	log_xi		1.91463	+/-	5.65348E-02
4	2	zxipcf	CvrFract		0.443201	+/-	2.00510E-02
5	2	zxipcf	Redshift		0.0	frozen	
6	3	diskbb	Tin	keV	0.949737	+/-	6.35650E-03
7	3	diskbb	norm		1.91127E+04	+/-	1444.61
8	4	relxill	Index1		10.0000	+/-	16.4329
9	4	relxill	Index2		2.00000E-07	frozen	
10	4	relxill	Rbr		9.80774	+/-	12.6059
11	4	relxill	a		0.911651	+/-	0.296701
12	4	relxill	Incl	deg	66.4794	+/-	5.63955
13	4	relxill	Rin		-1.10183	+/-	0.723351
14	4	relxill	Rout		400.000	frozen	
15	4	relxill	z		0.0	frozen	
16	4	relxill	gamma		3.38026	+/-	0.732087
17	4	relxill	logxi		2.99824	+/-	1.49570
18	4	relxill	Afe		10.0000	+/-	18.6973
19	4	relxill	Ecut	keV	25.7943	+/-	33.8038
20	4	relxill	refl_frac		9.92469	+/-	10.9701
21	4	relxill	norm		0.252989	+/-	0.329496
Data group: 2							
22	1	TBabs	nH	10^22	0.217273	= p1	
23	2	zxipcf	Nh	10^22	38.8523	= p2	
24	2	zxipcf	log_xi		1.91463	= p3	
25	2	zxipcf	CvrFract		0.443201	= p4	
26	2	zxipcf	Redshift		0.0	= p5	
27	3	diskbb	Tin	keV	0.949737	= p6	
28	3	diskbb	norm		1.83106E+04	+/-	1384.49
29	4	relxill	Index1		10.00000	= p8	
30	4	relxill	Index2		2.00000E-07	= p9	
31	4	relxill	Rbr		9.80774	= p10	
32	4	relxill	a		0.911651	= p11	
33	4	relxill	Incl	deg	66.4794	= p12	
34	4	relxill	Rin		-1.10183	= p13	
35	4	relxill	Rout		400.000	= p14	
36	4	relxill	z		0.0	= p15	
37	4	relxill	gamma		3.38026	= p16	
38	4	relxill	logxi		2.99824	= p17	
39	4	relxill	Afe		10.0000	= p18	
40	4	relxill	Ecut	keV	25.7943	= p19	
41	4	relxill	refl_frac		9.92469	= p20	
42	4	relxill	norm		0.243270	+/-	0.316877

Fit statistic : Chi-Squared = 566.02 using 379 PHA bins.

Test statistic : Chi-Squared = 566.02 using 379 PHA bins.
Reduced chi-squared = 1.5723 for 360 degrees of freedom

Figure 5.6: Parameters of 80702317006

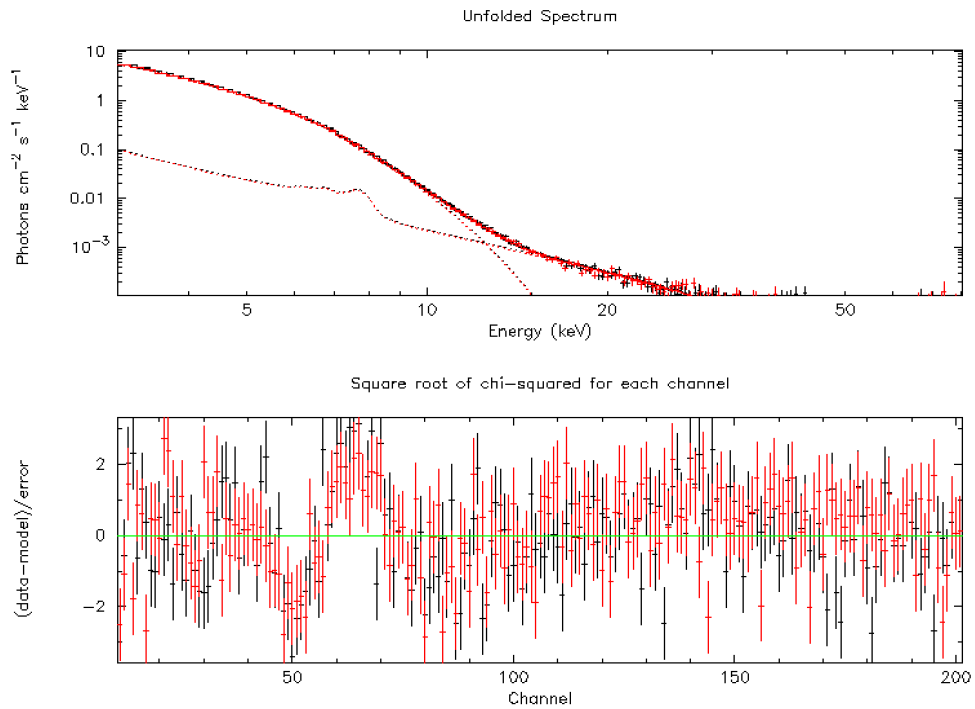


Figure 5.7: Plot of 80702317006

Parameter	Confidence Range (1)
1	0.217263 0.217273 (-9.7885e-06, 1.44117e-09)
2	38.8491 38.8523 (-0.0031638, -1.79333e-08)
3	1.91463 1.91489 (1.41855e-08, 0.000256131)
4	0.443175 0.443201 (-2.60726e-05, -1.7782e-08)
6	0.949484 0.949737 (-0.0002531, -3.36738e-08)
7	19112.7 19112.8 (-0.0512438, 0.0930928)
8	9.99896 10 (-0.00104408, -2.30362e-06)
10	9.80768 9.80779 (-5.63008e-05, 5.11932e-05)
11	0.911569 0.911651 (-8.24309e-05, 1.72823e-11)
12	66.4794 66.4827 (2.147e-07, 0.00325419)
13	-1.1019 -1.10183 (-6.57312e-05, 4.0318e-10)
16	3.38025 3.38028 (-5.60357e-06, 1.67739e-05)
17	2.99733 2.99824 (-0.000912291, -3.80852e-07)
18	10 10 (0, 0)
19	25.7934 25.7943 (-0.000864658, -1.97472e-07)
20	9.92298 9.92469 (-0.0017069, -4.0987e-07)
21	0.252804 0.252989 (-0.00018515, -2.71466e-08)
28	18308.5 18310.6 (-2.0723, -0.000887702)
42	0.243267 0.243271 (-2.73365e-06, 7.84724e-07)

Figure 5.8: Error of 80702317006

```

Data group: 1
 1  1  TBabs      nH      10^22    1.36420      +/-  0.280632
 2  2  zxipcf      Nh      10^22    47.4111     +/-  5.28280
 3  2  zxipcf      log_xi   1.88638     +/-  0.404080
 4  2  zxipcf      CvrFract 0.464703     +/-  5.83247E-02
 5  2  zxipcf      Redshift 0.0          frozen
 6  3  diskbb      Tin      keV     0.897519     +/-  1.07616E-02
 7  3  diskbb      norm     2.39528E+04  +/-  3760.88
 8  4  relxill     Index1   5.79864     +/-  2.87479
 9  4  relxill     Index2   2.00000E-07  frozen
10  4  relxill     Rbr     68.3838     +/-  7848.83
11  4  relxill     a       0.949889     +/-  0.145097
12  4  relxill     Incl    deg     66.5725     +/-  1.78206
13  4  relxill     Rin     -1.13084    +/-  0.605631
14  4  relxill     Rout    400.000     frozen
15  4  relxill     z       0.0          frozen
16  4  relxill     gamma   2.74397     +/-  1.14653
17  4  relxill     logxi   2.29730     +/-  1.02672
18  4  relxill     Afe    10.0000     +/-  15.1484
19  4  relxill     Ecut    keV     5.82976     +/-  1.69752
20  4  relxill     refl_frac 18.6804     +/-  29.6195
21  4  relxill     norm    4.33523E-02  +/-  0.149045

Data group: 2
22  1  TBabs      nH      10^22    1.36420      = p1
23  2  zxipcf      Nh      10^22    47.4111     = p2
24  2  zxipcf      log_xi   1.88638     = p3
25  2  zxipcf      CvrFract 0.464703     = p4
26  2  zxipcf      Redshift 0.0          = p5
27  3  diskbb      Tin      keV     0.897519     = p6
28  3  diskbb      norm     2.29186E+04  +/-  3597.29
29  4  relxill     Index1   5.79864     = p8
30  4  relxill     Index2   2.00000E-07  = p9
31  4  relxill     Rbr     68.3838     = p10
32  4  relxill     a       0.949889    = p11
33  4  relxill     Incl    deg     66.5725     = p12
34  4  relxill     Rin     -1.13084    = p13
35  4  relxill     Rout    400.000     = p14
36  4  relxill     z       0.0          = p15
37  4  relxill     gamma   2.74397     = p16
38  4  relxill     logxi   2.29730     = p17
39  4  relxill     Afe    10.0000     = p18
40  4  relxill     Ecut    keV     5.82976     = p19
41  4  relxill     refl_frac 18.6804     = p20
42  4  relxill     norm    4.23174E-02  +/-  0.145458

Using energies from responses.

Fit statistic : Chi-Squared =      508.56 using 361 PHA bins.

Test statistic : Chi-Squared =      508.56 using 361 PHA bins.
Reduced chi-squared = 1.4870 for 342 degrees of freedom

```

Figure 5.9: Parameters of 80702317008

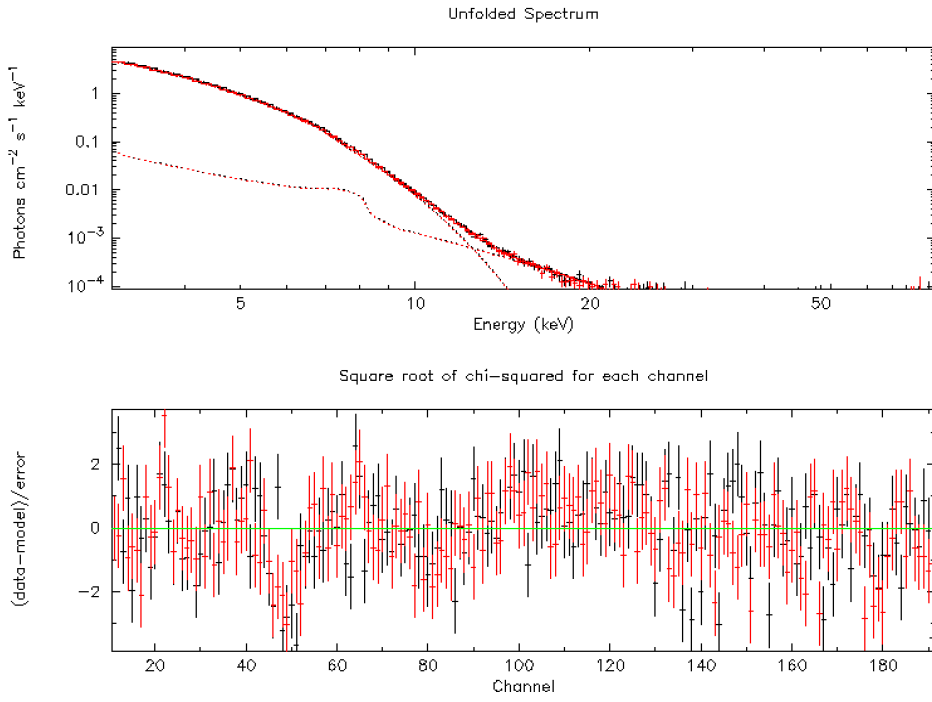


Figure 5.10: Plot of 80702317008

Errors calculated from chains			
Parameter	Confidence Range (1)		
1	1.3609	1.37771	(-0.00330222, 0.0135035)
2	47.3513	47.561	(-0.0598069, 0.149852)
3	1.87567	1.89355	(-0.0107187, 0.00716607)
4	0.464141	0.465422	(-0.000561354, 0.000719633)
6	0.896381	0.897584	(-0.00113845, 6.42568e-05)
7	23939.9	24194	(-12.9676, 241.113)
8	5.77553	5.80929	(-0.023109, 0.0106582)
10	68.2887	68.5598	(-0.0950796, 0.175945)
11	0.933957	0.952444	(-0.0159316, 0.0025554)
12	65.8207	66.6295	(-0.751884, 0.057001)
13	-1.15031	-1.11533	(-0.0194734, 0.0155094)
16	2.73961	2.74946	(-0.00436205, 0.00548307)
17	2.2765	2.29994	(-0.0207969, 0.00264162)
18	10	10	(0, 0)
19	5.79796	5.85627	(-0.0317968, 0.026514)
20	18.6544	18.7356	(8.64065, 8.72179)
21	0.0433228	0.0436507	(-2.95317e-05, 0.000298418)
28	22896.9	23154.6	(-21.6661, 236.024)
42	0.0420437	0.0423281	(-0.000273646, 1.07911e-05)

Figure 5.11: Errors of 80702317008

Data group: 1							
1	1	TBabs	nH	10^{22}	0.644000	+/-	0.349010
2	2	zxipcf	Nh	10^{22}	34.2144	+/-	7.02660
3	2	zxipcf	log_xi		1.43561	+/-	0.360976
4	2	zxipcf	CvrFract		0.449005	+/-	3.68142E-02
5	2	zxipcf	Redshift		0.0	frozen	
6	3	diskbb	Tin	keV	0.809069	+/-	9.86159E-03
7	3	diskbb	norm		1.83504E+04	+/-	2299.62
8	4	relxill	Index1		4.89815	+/-	2.71444
9	4	relxill	Index2		2.00000E-07	frozen	
10	4	relxill	Rbr		29.7091	+/-	33.1019
11	4	relxill	a		0.952703	+/-	0.221910
12	4	relxill	Incl	deg	63.8856	+/-	2.36033
13	4	relxill	Rin		-1.00976	+/-	0.830093
14	4	relxill	Rout		400.000	frozen	
15	4	relxill	z		0.0	frozen	
16	4	relxill	gamma		2.34198	+/-	0.421344
17	4	relxill	logxi		1.00000E-06	frozen	
18	4	relxill	Afe		10.0000	+/-	16.2965
19	4	relxill	Ecut	keV	78.8725	+/-	85.1054
20	4	relxill	refl_frac		1.94836	+/-	0.985121
21	4	relxill	norm		1.02718E-02	+/-	9.89651E-03
Data group: 2							
22	1	TBabs	nH	10^{22}	0.644000	= p1	
23	2	zxipcf	Nh	10^{22}	34.2144	= p2	
24	2	zxipcf	log_xi		1.43561	= p3	
25	2	zxipcf	CvrFract		0.449005	= p4	
26	2	zxipcf	Redshift		0.0	= p5	
27	3	diskbb	Tin	keV	0.809069	= p6	
28	3	diskbb	norm		1.78872E+04	+/-	2240.96
29	4	relxill	Index1		4.89815	= p8	
30	4	relxill	Index2		2.00000E-07	= p9	
31	4	relxill	Rbr		29.7091	= p10	
32	4	relxill	a		0.952703	= p11	
33	4	relxill	Incl	deg	63.8856	= p12	
34	4	relxill	Rin		-1.00976	= p13	
35	4	relxill	Rout		400.000	= p14	
36	4	relxill	z		0.0	= p15	
37	4	relxill	gamma		2.34198	= p16	
38	4	relxill	logxi		1.00000E-06	= p17	
39	4	relxill	Afe		10.0000	= p18	
40	4	relxill	Ecut	keV	78.8725	= p19	
41	4	relxill	refl_frac		1.94836	= p20	
42	4	relxill	norm		1.02110E-02	+/-	9.83458E-03

Fit statistic : Chi-Squared = 445.59 using 412 PHA bins.

Figure 5.12: Parameters of 90702326002

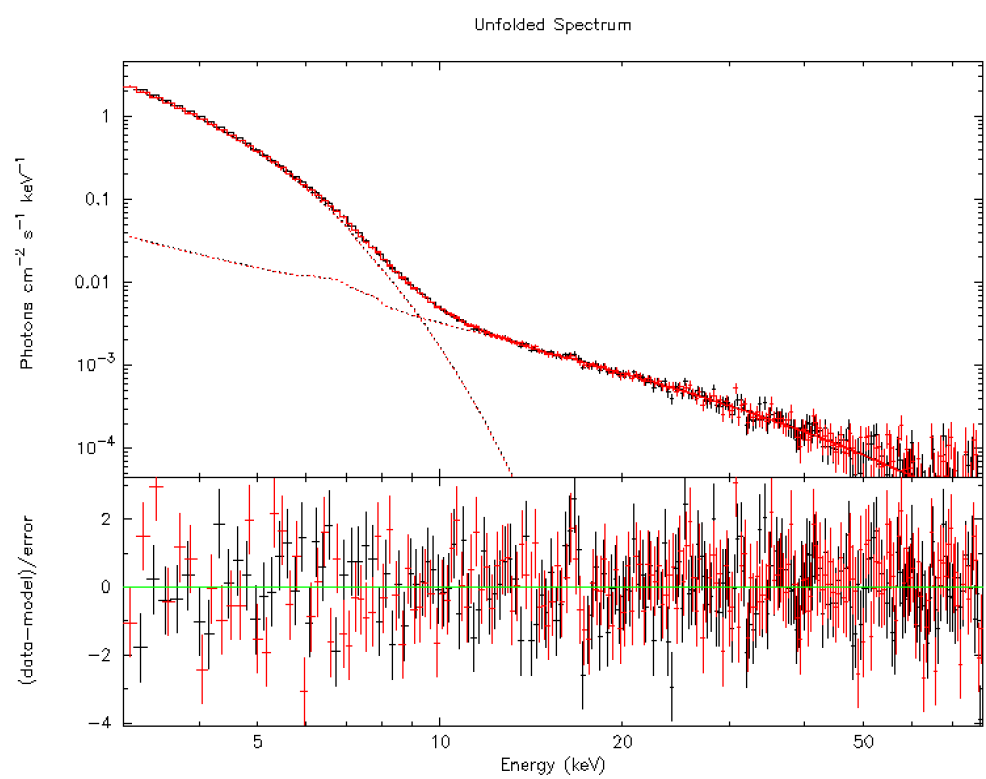


Figure 5.13: Plot of 90702326002

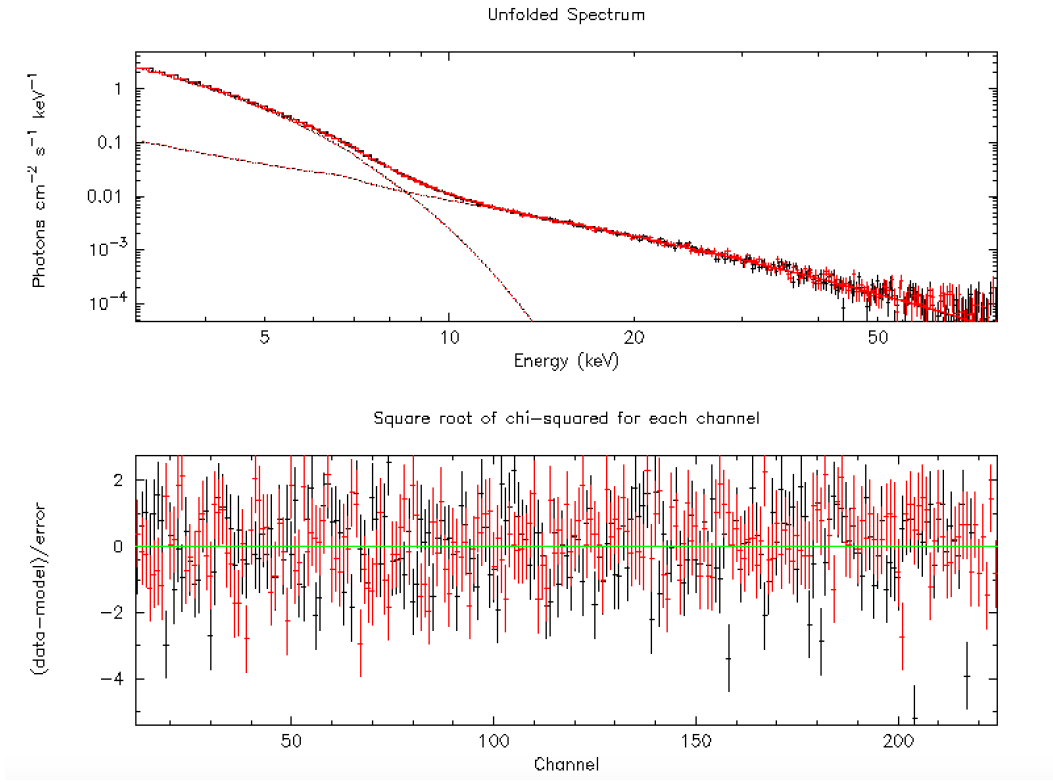
5.5.6 90702326004

Below are the produced parameters for the best fit obtained.

Data group: 1						
1	1	TBabs	nH	10^22	0.413944	+/- 0.538336
2	2	zxicpf	Nh	10^22	36.1149	+/- 5.73474
3	2	zxicpf	log_xi		0.749080	+/- 0.987393
4	2	zxicpf	CvrFract		0.420581	+/- 0.177653
5	2	zxicpf	Redshift		0.0	frozen
6	3	diskbb	Tin	keV	0.844763	+/- 3.30656E-02
7	3	diskbb	norm		1.53331E+04	+/- 8275.61
8	4	relxill	Index1		10.0000	+/- 29.9748
9	4	relxill	Index2		4.00000E-07	frozen
10	4	relxill	Rbr		38.5561	+/- 2929.84
11	4	relxill	a		0.989385	+/- 1.88412E-02
12	4	relxill	Incl	deg	70.0227	+/- 16.8044
13	4	relxill	Rin		-1.13138	+/- 0.360509
14	4	relxill	Rout		400.000	frozen
15	4	relxill	z		0.0	frozen
16	4	relxill	gamma		2.46900	+/- 0.377672
17	4	relxill	logxi		2.10710	+/- 6.40667
18	4	relxill	Afe		10.0000	+/- 28.8113
19	4	relxill	Ecut	keV	89.0059	+/- 97.4564
20	4	relxill	refl_frac		1.37576	+/- 4.32678
21	4	relxill	norm		3.77688E-02	+/- 3.73374E-02
Data group: 2						
22	1	TBabs	nH	10^22	0.413944	= p1
23	2	zxicpf	Nh	10^22	36.1149	= p2
24	2	zxicpf	log_xi		0.749080	= p3
25	2	zxicpf	CvrFract		0.420581	= p4
26	2	zxicpf	Redshift		0.0	= p5
27	3	diskbb	Tin	keV	0.844763	= p6
28	3	diskbb	norm		1.49707E+04	+/- 8082.97
29	4	relxill	Index1		10.0000	= p8
30	4	relxill	Index2		4.00000E-07	= p9
31	4	relxill	Rbr		38.5561	= p10
32	4	relxill	a		0.989385	= p11
33	4	relxill	Incl	deg	70.0227	= p12
34	4	relxill	Rin		-1.13138	= p13
35	4	relxill	Rout		400.000	= p14
36	4	relxill	z		0.0	= p15
37	4	relxill	gamma		2.46900	= p16
38	4	relxill	logxi		2.10710	= p17
39	4	relxill	Afe		10.0000	= p18
40	4	relxill	Ecut	keV	89.0059	= p19
41	4	relxill	refl_frac		1.37576	= p20
42	4	relxill	norm		3.81955E-02	+/- 3.77569E-02

Using energies from responses.
Fit statistic : Chi-Squared = 504.74 using 420 PHA bins.
Test statistic : Chi-Squared = 504.74 using 420 PHA bins.

The modeled spectrum.



5.5.7 90702326006

This was the first observation that was studied in the research paper from the source 4U 1543-47. The scientists had already computed the parameter values after obtaining the best fit. I used these values as a reference(initial input) to obtain the best possible fit myself along with parameter values that were in close proximity with their values. Below you can see the parameter values. The value after the +/- symbol represents the step size in which the parameter value can vary during the fitting process. Now I will show what the spectral data looks like after modelling. Look at the below figure. The above plot would have given you a better idea.

Next, we will talk about the error computation which was done using the MCMC chain method. Over here time is a big issue as the software will take time to build a long chain if you don't have good enough computational power. In this observation, the chain length was set as 2000000 with the burn in phase set as 50000. The below are the error values with 1 sigma confidence values. The rightmost column gives the range of error values for that parameter from the mean/actual value. The second and third column gives the min-

Data group: 1							
1	1	TBabs	nH	10^22	1.80486	+/-	0.231481
2	2	zxipcf	Nh	10^22	51.9948	+/-	2.97577
3	2	zxipcf	log_xi		1.94072	+/-	3.23721E-02
4	2	zxipcf	CvrFract		0.511117	+/-	1.56567E-02
5	2	zxipcf	Redshift		0.0	frozen	
6	3	diskbb	Tin	keV	0.807890	+/-	5.07730E-03
7	3	diskbb	norm		2.79700E+04	+/-	1741.91
8	4	relxill	Index1		8.50165	+/-	5.93823
9	4	relxill	Index2		2.00000E-07	+/-	-1.00000
10	4	relxill	Rbr		25.4089	+/-	1612.01
11	4	relxill	a		0.969889	+/-	3.04685E-02
12	4	relxill	Incl	deg	67.3576	+/-	3.39647
13	4	relxill	Rin		-1.33977	+/-	0.204172
14	4	relxill	Rout		400.000	frozen	
15	4	relxill	z		0.0	frozen	
16	4	relxill	gamma		2.69671	+/-	0.411714
17	4	relxill	logxi		2.29731	+/-	0.660998
18	4	relxill	Afe		10.0000	+/-	11.4478
19	4	relxill	Ecut	keV	98.8879	+/-	119.052
20	4	relxill	refl_frac		3.08933	+/-	1.98580
21	4	relxill	norm		2.07723E-02	+/-	2.47001E-02
Data group: 2							
22	1	TBabs	nH	10^22	1.80486	= p1	
23	2	zxipcf	Nh	10^22	51.9948	= p2	
24	2	zxipcf	log_xi		1.94072	= p3	
25	2	zxipcf	CvrFract		0.511117	= p4	
26	2	zxipcf	Redshift		0.0	frozen	
27	3	diskbb	Tin	keV	0.807890	= p6	
28	3	diskbb	norm		2.72445E+04	+/-	1693.50
29	4	relxill	Index1		8.50165	= p8	
30	4	relxill	Index2		2.00000E-07	= p9	
31	4	relxill	Rbr		25.4089	= p10	
32	4	relxill	a		0.969889	= p11	
33	4	relxill	Incl	deg	67.3576	= p12	
34	4	relxill	Rin		-1.33977	= p13	
35	4	relxill	Rout		400.000	= p14	
36	4	relxill	z		0.0	frozen	
37	4	relxill	gamma		2.69671	= p16	
38	4	relxill	logxi		2.29731	= p17	
39	4	relxill	Afe		10.0000	= p18	
40	4	relxill	Ecut	keV	98.8879	= p19	
41	4	relxill	refl_frac		3.06990	+/-	1.97468
42	4	relxill	norm		2.10270E-02	+/-	2.50069E-02

| Fit statistic : Chi-Squared = 437.90 using 418 PHA bins.

Test statistic : Chi-Squared = 437.90 using 418 PHA bins.

Reduced chi-squared = 1.0866 for 403 degrees of freedom

Null hypothesis probability = 1.114264e-01

Figure 5.14: Parameters of 90702326006

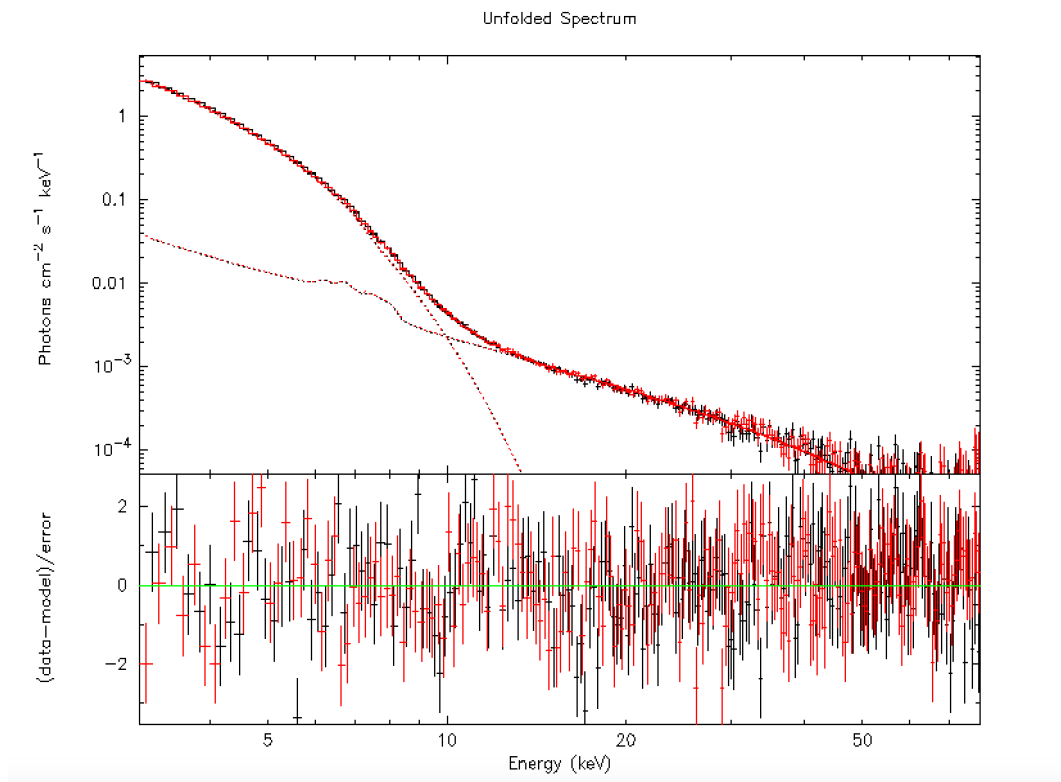


Figure 5.15: Plot of 90702326006

```

error 1.0 1 2 3 4 6 7 8 9 10 11 12 13 16 17 18 19 20 21 28 42
Errors calculated from chains
Parameter Confidence Range (1)
 1      1.00028      1.53953      (-0.804583,-0.265328)
 2      43.5908      49.1199      (-8.40404,-2.87494)
 3      1.90155      1.95795      (-0.0391687,0.0172329)
 4      0.502656      0.525812      (-0.00846138,0.0146949)
 6      0.807837      0.813027      (-5.23585e-05,0.00513732)
 7      25116.2      27066.6      (-2853.83,-903.438)
 8      3.94454      8.48594      (-4.55711,-0.0157139)
 9 -9.55052e-05  5.00232e-05      (-9.57052e-05,4.98232e-05)
10      25.5865      454.405      (0.17756,428.996)
11      0.907754      0.978042      (-0.0621358,0.00815235)
12      64.4173      67.0675      (-2.94034,-0.290095)
13     -1.40639      -1.06592      (-0.0666221,0.273852)
16      2.71494      2.88231      (0.0182329,0.185602)
17      2.16665      2.49835      (-0.130657,0.201042)
18      8.96138      9.91027      (-1.03862,-0.0897273)
19     107.982      342.746      (9.09451,243.858)
20      2.96003      3.73805      (-0.129296,0.648718)
21      0.0213363      0.0358678      (0.000564083,0.0150956)
28      24460.9      26357.1      (-2783.6,-887.456)
42      0.0215215      0.0362259      (0.000494472,0.0151989)

```

Figure 5.16: Error of 90702326006

imum and maximum value for that parameter value respectively. Hence the errors were computed.

5.5.8 90702326008

This is one of the four observations that were studied(namely the second) and researched upon in the **Draghis** paper. I had used the parameter values from the paper as a reference for my fitting procedure and my guide had approved of this. Below are the parameter values that I have obtained for best fit. This is the best fit that I have obtained. The reduced chi-squared value is pretty close to 1 as can be seen. A few parameters are frozen here for the same reason they were frozen before. Redshift has not been frozen here for trial purposes

Below is the modeled spectrum. For computing the errors I used the MCMC analysis like other data sets. For this, the maximum chain length that I could have set is 2000000 before the computer shows an error. The burn-in was set to 50000. Below are the error ranges that I obtained. The rightmost column gives the range of error values for that parameter from the mean/actual value. The second and third column gives the minimum and maximum value for that parameter value respectively.

5.5.9 90702326010

This was the third observation that was studied and researched in the paper. Again the parameter values from the paper were used as a source of reference under the guidance of my guide. Below are the following parameters that I obtained. This is the best fit that I have obtained for this observation after multiple tries. The chi-squared value obtained is decent over here. Some of the parameters are frozen for reasons mentioned in previous observations. Below is the plot of the modeled spectrum. Now I will display the error values that I have obtained for this observation, the chain length went up to 1000000 for a good result with the burn in phase set as 50000. Below are the error values with the confidence intervals. To specify these errors are calculated within 1 sigma confidence. The rightmost column gives the range of error values for that parameter from the mean/actual value. The second and third column gives the minimum and maximum value for that parameter value respectively.

Data group: 1						
1	1	TBabs	nH	10^{22}	0.366986	+/- 0.553111
2	2	zxipcf	Nh	10^{22}	36.6175	+/- 6.43628
3	2	zxipcf	log_xi		0.681428	+/- 1.12292
4	2	zxipcf	CvrFract		0.420796	+/- 0.178731
5	2	zxipcf	Redshift		1.68905E-02	+/- 9.08444E-03
6	3	diskbb	Tin	keV	0.844826	+/- 3.37264E-02
7	3	diskbb	norm		1.52618E+04	+/- 8419.43
8	4	relxill	Index1		9.79022	+/- 12.3765
9	4	relxill	Index2		4.00000E-07	frozen
10	4	relxill	Rbr		29.3359	+/- 146.399
11	4	relxill	a		0.963814	+/- 4.41212E-02
12	4	relxill	Incl	deg	65.7500	+/- 14.5715
13	4	relxill	Rin		-1.05511	+/- 0.324425
14	4	relxill	Rout		400.000	frozen
15	4	relxill	z		0.0	frozen
16	4	relxill	gamma		2.46905	+/- 0.331280
17	4	relxill	logxi		2.01173	+/- 3.70546
18	4	relxill	Afe		10.0000	+/- 14.4139
19	4	relxill	Ecut	keV	83.9159	+/- 65.3068
20	4	relxill	refl_frac		1.21835	+/- 1.81907
21	4	relxill	norm		3.75876E-02	+/- 3.44324E-02
Data group: 2						
22	1	TBabs	nH	10^{22}	0.366986	= p1
23	2	zxipcf	Nh	10^{22}	36.6175	= p2
24	2	zxipcf	log_xi		0.681428	= p3
25	2	zxipcf	CvrFract		0.420796	= p4
26	2	zxipcf	Redshift		1.68905E-02	= p5
27	3	diskbb	Tin	keV	0.844826	= p6
28	3	diskbb	norm		1.49010E+04	+/- 8223.97
29	4	relxill	Index1		9.79022	= p8
30	4	relxill	Index2		4.00000E-07	= p9
31	4	relxill	Rbr		29.3359	= p10
32	4	relxill	a		0.963814	= p11
33	4	relxill	Incl	deg	65.7500	= p12
34	4	relxill	Rin		-1.05511	= p13
35	4	relxill	Rout		400.000	= p14
36	4	relxill	z		0.0	= p15
37	4	relxill	gamma		2.46905	= p16
38	4	relxill	logxi		2.01173	= p17
39	4	relxill	Afe		10.0000	= p18
40	4	relxill	Ecut	keV	83.9159	= p19
41	4	relxill	refl_frac		1.21835	= p20
42	4	relxill	norm		3.80089E-02	+/- 3.47961E-02

Fit statistic : Chi-Squared = 498.80 using 420 PHA bins.

Test statistic : Chi-Squared = 498.80 using 420 PHA bins.
 Reduced chi-squared = 1.2470 for 400 degrees of freedom
 Null hypothesis probability = 5.490951e-04

Figure 5.17: Parameters of 90702326008

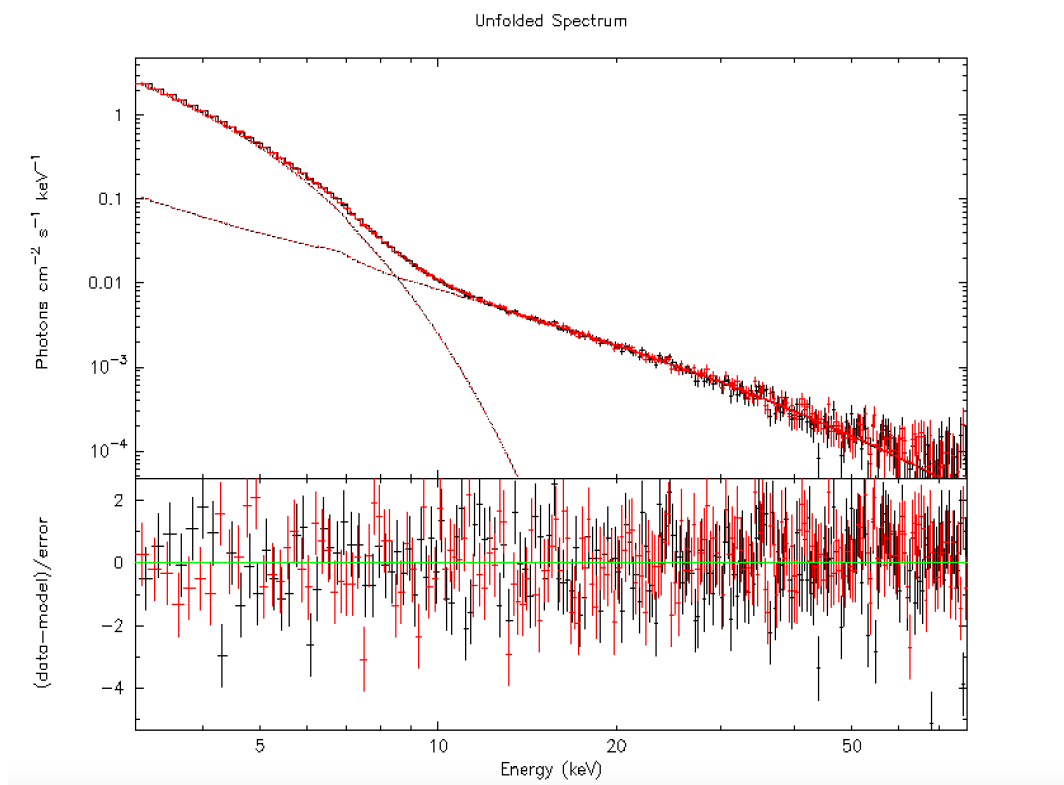


Figure 5.18: Plot of 90702326008

```

XSPEC12>error 1.0 1 2 3 4 5 6 7 8 10 11 12 13 16 17 18 19 20 21 28 42
Errors calculated from chains
Parameter  Confidence Range (1)
  1      0.230478    0.490556   (-0.136508,0.12357)
  2      34.8402     39.953     (-1.77732,3.33557)
  3      0.490515    1.06887    (-0.190913,0.387438)
  4      0.385019    0.442821   (-0.035777,0.0220252)
  5      0.0115361   0.0248434  (-0.00535436,0.00795286)
  6      0.84177     0.851686   (-0.00305601,0.00685979)
  7      13692.5     16188.4    (-1569.36,926.535)
  8      6.94498     9.68737    (-2.84524,-0.102854)
 10     31.2025     69.6567    (1.86663,40.3209)
 11     0.936984    0.980403   (-0.0268295,0.016589)
 12     57.3043     66.7752    (-8.4457,1.02518)
 13     -1.32992    -1.03117   (-0.274804,0.0239421)
 16     2.4616      2.56817   (-0.00744823,0.0991251)
 17     1.30929     2.37008   (-0.702441,0.358346)
 18     5.83702     9.53672   (-4.16298,-0.463284)
 19     84.0461     119.728   (0.130177,35.8117)
 20     0.884948    1.48168   (-0.333399,0.26333)
 21     0.0361275   0.0483604 (-0.00146013,0.0107728)
 28     13370.3     15804.5   (-1530.65,903.556)
 42     0.0364467   0.0488106 (-0.00156224,0.0108017)

```

Figure 5.19: Error of 90702326008

Data group: 1							
1	1	TBabs	nH	10^{22}	1.39297	+/-	0.375666
2	2	zxipcf	Nh	10^{22}	63.6799	+/-	18.6389
3	2	zxipcf	log_xi		2.20592	+/-	0.119772
4	2	zxipcf	CvrFract		0.396273	+/-	6.50652E-02
5	2	zxipcf	Redshift		0.0		frozen
6	3	diskbb	Tin	keV	0.817690	+/-	8.94157E-03
7	3	diskbb	norm		1.75176E+04	+/-	1963.06
8	4	relxill	Index1		8.11324	+/-	6.39658
9	4	relxill	Index2		1.00000E-07		frozen
10	4	relxill	Rbr		10.3005	+/-	10.0444
11	4	relxill	a		0.908259	+/-	0.464930
12	4	relxill	Incl	deg	68.0687	+/-	4.03878
13	4	relxill	Rin		-1.00961	+/-	1.10264
14	4	relxill	Rout		400.000		frozen
15	4	relxill	z		0.0		frozen
16	4	relxill	gamma		2.72567	+/-	0.308054
17	4	relxill	logxi		2.29699	+/-	0.549299
18	4	relxill	Afe		7.09015	+/-	5.83062
19	4	relxill	Ecut	keV	462.861	+/-	1798.56
20	4	relxill	refl_frac		2.43532	+/-	0.799463
21	4	relxill	norm		2.77248E-02	+/-	2.49750E-02
Data group: 2							
22	1	TBabs	nH	10^{22}	1.39297	= p1	
23	2	zxipcf	Nh	10^{22}	63.6799	= p2	
24	2	zxipcf	log_xi		2.20592	= p3	
25	2	zxipcf	CvrFract		0.396273	= p4	
26	2	zxipcf	Redshift		0.0	= p5	
27	3	diskbb	Tin	keV	0.817690	= p6	
28	3	diskbb	norm		1.71931E+04	+/-	1924.93
29	4	relxill	Index1		8.11324	= p8	
30	4	relxill	Index2		1.00000E-07	= p9	
31	4	relxill	Rbr		10.3005	= p10	
32	4	relxill	a		0.908259	= p11	
33	4	relxill	Incl	deg	68.0687	= p12	
34	4	relxill	Rin		-1.00961	= p13	
35	4	relxill	Rout		400.000	= p14	
36	4	relxill	z		0.0	= p15	
37	4	relxill	gamma		2.72567	= p16	
38	4	relxill	logxi		2.29699	= p17	
39	4	relxill	Afe		7.09015	= p18	
40	4	relxill	Ecut	keV	462.861	= p19	
41	4	relxill	refl_frac		2.43532	= p20	
42	4	relxill	norm		2.81013E-02	+/-	2.52973E-02

Fit statistic : Chi-Squared = 512.48 using 419 PHA bins.

Test statistic : Chi-Squared = 512.48 using 419 PHA bins.

Reduced chi-squared = 1.2812 for 400 degrees of freedom

Null hypothesis probability = 1.173404e-04

Figure 5.20: Parameters of 90702326010

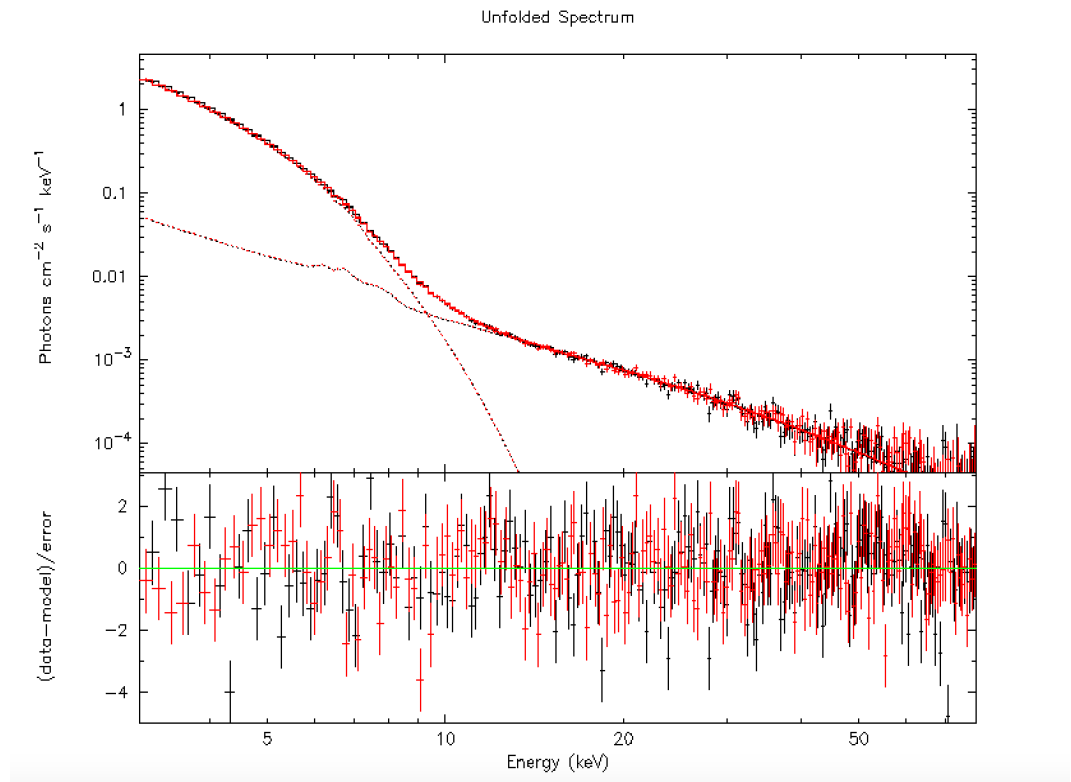


Figure 5.21: Plot of 90702326010

Parameter	Confidence	Range (1)
1	0.854931	1.46243 (-0.538045, 0.0694563)
2	44.8088	63.1196 (-18.8711, -0.560226)
3	1.96686	2.16534 (-0.239064, -0.040579)
4	0.409803	0.487801 (0.0135298, 0.0915281)
6	0.805156	0.816765 (-0.0125338, -0.000924756)
7	17936.6	21023.9 (418.923, 3506.28)
8	7.20856	9.25295 (-0.904691, 1.1397)
9	-3.28175e-07	5.21524e-07 (-4.28175e-07, 4.21524e-07)
10	9.63169	15.1389 (-0.668859, 4.83837)
11	0.883114	0.957137 (-0.0251436, 0.0488798)
12	65.2802	68.5796 (-2.78858, 0.510794)
13	-1.25549	-1.03152 (-0.245891, -0.0219284)
16	2.67998	2.75301 (-0.0456837, 0.0273382)
17	1.90959	2.40862 (-0.387358, 0.111663)
18	5.67575	8.61917 (-1.41439, 1.52903)
19	367.736	793.55 (-95.121, 330.693)
20	1.99257	2.55172 (-0.44276, 0.11639)
21	0.0244655	0.0307227 (-0.00325932, 0.0029979)
28	17605	20636.9 (411.874, 3443.73)
42	0.0248195	0.031128 (-0.00328177, 0.00302672)

Figure 5.22: Error of 90702326010

5.5.10 90702326012

This is the fourth observation that was studied and researched in the research paper. I used the parameter values as a reference under the guidance of my supervisor. Below are the parameter values that I obtained for the best fit. The values that I have obtained are similar(nearby) to those given in the paper. Below is the modeled spectrum. The value of logxi is a bit absurd but a better value could not have been obtained. The above image shows the error intervals using the MCMC analysis which were calculated like they were for the previous parameters. It was a long task which required patience. The chain length was set to 1000000 as the PC was not able to accurately compute higher chain lengths. The burn-in phase was set to 50000.

```

Data group: 1
 1  1  TBabs      nH      10^22   0.920596    +/-  0.287228
 2  2  zxipcf      Nh      10^22   45.7883     +/-  6.35909
 3  2  zxipcf      log_xi   1.87493     +/-  0.449141
 4  2  zxipcf      CvrFract 0.449869     +/-  5.77159E-02
 5  2  zxipcf      Redshift 0.0          frozen
 6  3  diskbb      Tin      keV    0.811816     +/-  1.04764E-02
 7  3  diskbb      norm     1.85067E+04  +/-  2968.37
 8  4  relxill     Index1   7.89015     +/-  25.7225
 9  4  relxill     Index2   2.00000E-07  frozen
10  4  relxill     Rbr      15.0231     +/-  82.6012
11  4  relxill     a        0.812540     +/-  2.07596
12  4  relxill     Incl     deg    64.6958     +/-  13.9294
13  4  relxill     Rin      -1.00000    +/-  6.09834
14  4  relxill     Rout     400.000    frozen
15  4  relxill     z        0.0          frozen
16  4  relxill     gamma    2.36192     +/-  0.426435
17  4  relxill     logxi   3.31686E-07  +/-  -1.00000
18  4  relxill     Afe     7.98946     +/-  7.98334
19  4  relxill     Ecut     keV    95.5497     +/-  125.529
20  4  relxill     refl_frac 1.39300     +/-  0.913525
21  4  relxill     norm     1.09952E-02  +/-  1.09789E-02

Data group: 2
22  1  TBabs      nH      10^22   0.920596    = p1
23  2  zxipcf      Nh      10^22   45.7883     = p2
24  2  zxipcf      log_xi   1.87493     = p3
25  2  zxipcf      CvrFract 0.449869     = p4
26  2  zxipcf      Redshift 0.0          = p5
27  3  diskbb      Tin      keV    0.811816     = p6
28  3  diskbb      norm     1.80420E+04  +/-  2892.20
29  4  relxill     Index1   7.89015     = p8
30  4  relxill     Index2   2.00000E-07  = p9
31  4  relxill     Rbr      15.0231     = p10
32  4  relxill     a        0.812540     = p11
33  4  relxill     Incl     deg    64.6958     = p12
34  4  relxill     Rin      -1.00000    = p13
35  4  relxill     Rout     400.000    = p14
36  4  relxill     z        0.0          = p15
37  4  relxill     gamma    2.36192     = p16
38  4  relxill     logxi   3.31686E-07  = p17
39  4  relxill     Afe     7.98946     = p18
40  4  relxill     Ecut     keV    95.5497     = p19
41  4  relxill     refl_frac 1.39300     = p20
42  4  relxill     norm     1.09366E-02  +/-  1.09159E-02

-----
Fit statistic : Chi-Squared =           448.31 using 412 PHA bins.

Test statistic : Chi-Squared =           448.31 using 412 PHA bins.
Reduced chi-squared =           1.1407 for   393 degrees of freedom
Null hypothesis probability = 2.801885e-02

```

Figure 5.23: Parameters of 90702326010

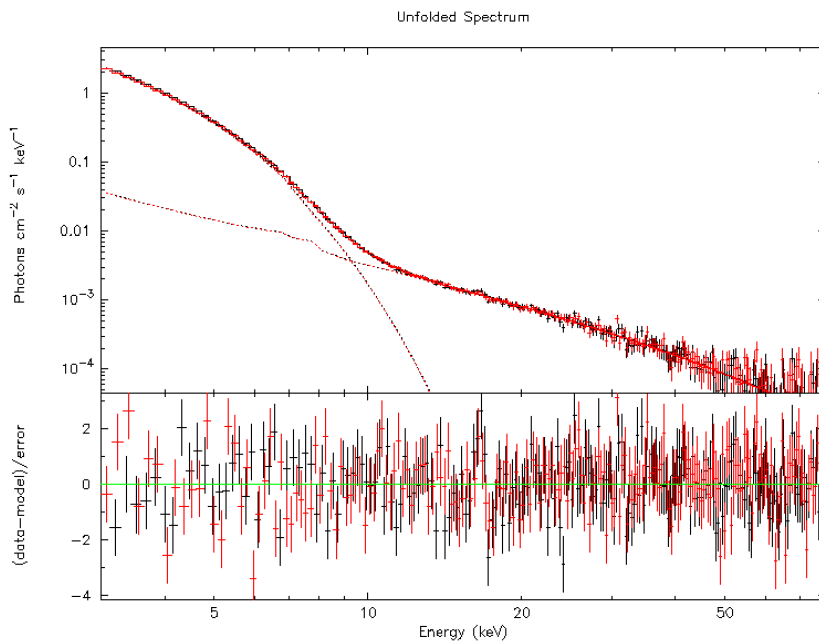


Figure 5.24: plot of 90702326012

Parameter	Confidence Range (1)
1	0.854931 1.46243 (-0.538045, 0.0694563)
2	44.8088 63.1196 (-18.8711, -0.560226)
3	1.96686 2.16534 (-0.239064, -0.040579)
4	0.409803 0.487801 (0.0135298, 0.0915281)
6	0.805156 0.816765 (-0.0125338, -0.000924756)
7	17936.6 21023.9 (418.923, 3506.28)
8	7.20856 9.25295 (-0.904691, 1.1397)
9	-3.28175e-07 5.21524e-07 (-4.28175e-07, 4.21524e-07)
10	9.63169 15.1389 (-0.668859, 4.83837)
11	0.883114 0.957137 (-0.0251436, 0.0488798)
12	65.2802 68.5796 (-2.78858, 0.510794)
13	-1.25549 -1.03152 (-0.245891, -0.0219284)
16	2.67998 2.75301 (-0.0456837, 0.0273382)
17	1.90959 2.40862 (-0.387358, 0.111663)
18	5.67575 8.61917 (-1.41439, 1.52903)
19	367.736 793.55 (-95.121, 330.693)
20	1.99257 2.55172 (-0.44276, 0.11639)
21	0.0244655 0.0307227 (-0.00325932, 0.0029979)
28	17605 20636.9 (411.874, 3443.73)
42	0.0248195 0.031128 (-0.00328177, 0.00302672)

Figure 5.25: error of 90702326012

Chapter 6

Bibliography and References

Here are the following links from which I have taken images and information. I will include research papers as well.

- https://en.wikipedia.org/wiki/X-ray_binary
- <https://heasarc.gsfc.nasa.gov/xanadu/xspec/>
- <https://heasarc.gsfc.nasa.gov/docs/binary.html>
- <https://www.sternwarte.uni-erlangen.de/~dauser/research/relxill/>
- <https://www.jpl.nasa.gov/missions/nuclear-spectroscopic-telescope->
- https://www-xray.ast.cam.ac.uk/xray_introduction/History.html
- A Systematic View of Ten New Black Hole Spins: Paper produced by Paul A. Draghis¹, Jon M. Miller¹, Abderahmen Zoghbi^{2,3,4}, Mark Reynolds^{1,5}, Elisa Costantini^{6,7}, Luigi C. Gallo⁸, and John A. Tomsick⁹
- Spectral Comparisons of Neutron Star Low-Mass X-Ray Binaries with Black Hole X-Ray Binaries: Paper produced by Prof. Luciano Burderi, Dr. Tiziana Di Salvo (Università degli Studi di Cagliari)
- IMPROVED REFLECTION MODELS OF BLACK HOLE ACCRETION DISKS: TREATING THE ANGULAR DISTRIBUTION OF X-RAYS J. García¹, T. Dauser², A. Lohfink^{3,4}, T. R. Kallman⁵, J. F. Steiner¹, J. E. McClintock¹, L. Brenneman¹, J. Wilms², W. Eikmann², C. S. Reynolds^{3,4}

- Astronomy and Astrophysics Abstracts (AAA, volume 67) by G. Burkhardt, U. Esser, H. Hefele, I. Heinrich, W. Hofmann, V. R. Matas, L. D. Schmadel, R. Wielen, G. Zech

Chapter 7

Conclusions

This internship under the guidance of Dr.Sami Mandal has give me a lot of insight about the area of X-Ray Binaries. The theory of the subject was of absolute interest to me. I had also gotten a chance to explore the software XSPEC during the internship which was of great help to me in my current semester. Producing whatever results I could took a long time of rigorous and repetitive efforts.

In the end I have computed the best fits, plots and errors for all observations which gave us a better idea about the source. My main aim was to estimate the spin parameter of the blackhole as that is of utmost importance to us compared to the other parameters. The observed reduced chi-squared ratios for some observations are not very close to one in my fitting procedure, but it was the best obtained by me in the given time frame and conditions. The errors also give us an idea about the parameters. The MCMC analysis was used instead of the normal error analysis method as that was done in the paper as well, and no one else in IIST had performed error analysis using that.

